The impact of ionized outflows from $z \sim 2.5$ quasars is not through instantaneous *in situ* quenching: the evidence from ALMA and VLT/SINFONI

J. Scholtz [1,2]★ C. M. Harrison [3]★ D. J. Rosario,[2] D. M. Alexander,[2] K. K. Knudsen [1] F. Stanley [1]
Chian-Chou Chen [4] D. Kakkad,[5] V. Mainieri[6] and J. Mullaney[7]

[1]*Department of Space, Earth and Environment, Onsala Space Observatory, Chalmers University of Technology, SE-439 92 Onsala, Sweden*
[2]*Department of Physics, Centre for Extragalactic Astronomy, Durham University, South Road, Durham DH1 3LE, UK*
[3]*School of Mathematics, Statistics and Physics, Newcastle University, Newcastle upon Tyne NE1 7RU, UK*
[4]*Academia Sinica Institute of Astronomy and Astrophysics (ASIAA), No. 1, Section 4, Roosevelt Rd., Taipei 10617, Taiwan*
[5]*European Southern Observatory, Alonso de Cordova 3107, Vitacura, Casilla 19001, Santiago de Chile, Chile*
[6]*European Southern Observatory, Karl-Schwarzschild-Strasse 2, Garching bei München, D-85748, Germany*
[7]*Department of Physics and Astronomy, University of Sheffield, Sheffield S3 7RH, UK*

ABSTRACT

We present high-resolution ($\sim$2.4 kpc) ALMA band 7 observations (rest-frame $\lambda \sim 250\,\mu$m) of three powerful $z \sim 2.5$ quasars ($L_{\rm bol} = 10^{47.3}$–$10^{47.5}$ erg s^{-1}). These targets have previously been reported as showing evidence for suppressed star formation based on cavities in the narrow Hα emission at the location of outflows traced with [O III] emission. Here, we combine the ALMA observations with a re-analysis of the VLT/SINFONI data to map the rest-frame far-infrared emission, Hα emission, and [O III] emission. In all targets, we observe high velocity [O III] gas (i.e. W80 $\sim$ 1000–2000 km s^{-1}) across the whole galaxy. We do not identify any Hα emission that is free from contamination from AGN-related processes; however, based on SED analyses, we show that the ALMA data contain a significant dust-obscured star formation component in two out of the three systems. This dust emission is found to be extended over $\approx$1.5–5.5 kpc in the nuclear regions, overlaps with the previously reported Hα cavities and is co-spatial with the peak in surface brightness of the [O III] outflows. In summary, within the resolution and sensitivity limits of the data, we do not see any evidence for a instantaneous shut down of *in situ* star formation caused directly by the outflows. However, similar to the conclusions of previous studies and based on our measured star formation rates, we do not rule out that the global host galaxy star formation could be suppressed on longer time-scales by the cumulative effect of quasar episodes during the growth of these massive black holes.

Key words: galaxies: active – galaxies: evolution – infrared: galaxies – X-rays: galaxies.

1 INTRODUCTION

It is now accepted that inside every massive galaxy resides a supermassive black hole (Kormendy & Ho 2013). During the growth of these supermassive black holes, via accretion events, these objects become visible as active galactic nuclei (AGN; Soltan 1982; Merloni, Rudnick & Di Matteo 2004). Current theoretical models of galaxy evolution require AGN to inject significant energy into their host galaxies in order to reproduce the basic properties of local galaxies and the intergalactic medium (IGM), such as the steep mass function, the black hole–spheroid relationships, increased width of specific star formation rate (SFR) distributions as a function of stellar mass, galaxy sizes, galaxy colour bi-modality, AGN number densities and enrichment of the IGM by metals (e.g. Silk & Rees 1998; Di Matteo, Springel & Hernquist 2005; Alexander & Hickox 2012; Dubois et al.

2013a,b; Hirschmann et al. 2014; Vogelsberger et al. 2014; Crain et al. 2015; Segers et al. 2016; Beckmann et al. 2017; Harrison 2017; Choi et al. 2018; Scholtz et al. 2018). In these models, the AGN are required to regulate the cooling of the interstellar medium (ISM) and/or intracluster medium or to eject gas out of the galaxy through galactic wide outflows. This process is usually referred to as 'AGN feedback', and it is believed to regulate the rate at which stars can form. However, from an observational perspective, it is still not clear what role AGN play in regulating star formation in the overall galaxy population, especially at high redshift and for the most radiatively powerful AGN called quasars (e.g. Harrison 2017; Cresci & Maiolino 2018).

Over the past decade, many studies have focused on identifying and characterizing multiphase outflows in galaxies (see e.g. Fiore et al. 2017; Cicone et al. 2018; Harrison et al. 2018; Veilleux et al. 2020). Indeed, there is now significant evidence that energetic ionized, atomic, and molecular outflows are commonly found in AGN host galaxies across a wide range of cosmic epochs (e.g. Morganti, Tadhunter & Oosterloo 2005; Veilleux, Cecil & Bland-

★ E-mail: honzascholtz@gmail.com (JH);
Christopher.Harrison@newcastle.ac.uk (CMH)

Hawthorn 2005; Ganguly & Brotherton 2008; Sturm et al. 2011; Cicone et al. 2012; Harrison et al. 2012; Cicone et al. 2014; Zakamska & Greene 2014; Balmaverde & Capetti 2015; Brusa et al. 2015; Carniani et al. 2015; Woo et al. 2016; Harrison et al. 2016a; Leung et al. 2017; Brusa et al. 2018; Lansbury et al. 2018; Förster Schreiber et al. 2018a; Fluetsch et al. 2019; Husemann et al. 2019; Perna et al. 2019; Ramos Almeida et al. 2019). Furthermore, these AGN-driven outflows have been identified on a large range of spatial scales (between tens of parsecs to tens of kiloparsecs; e.g. Storchi-Bergmann et al. 2010; Veilleux et al. 2013; Carniani et al. 2015; Cresci et al. 2015b; Feruglio et al. 2015; Kakkad et al. 2016; McElroy et al. 2016; Rupke, Gültekin & Veilleux 2017; Jarvis et al. 2019; Kakkad et al. 2020). Given that these outflows can be located on these scales, they may have the potential to impact upon the ISM and, consequently, the star formation inside the host galaxies.

Despite observations showing that AGN outflows are common, and can extend over large scales, the impact that they have on star formation is still open to debate. For example, statistical, non-spatially resolved, studies in the literature provide contradictory conclusions on the relationship between ionized outflows and the SFRs of the host galaxies (Balmaverde et al. 2016; Wylezalek & Zakamska 2016; Woo, Son & Bae 2017; Woo, Son & Rakshit 2020). In many of the spatially resolved studies, the most powerful outflows are capable of removing or destroying at least some of the star-forming material at a rate faster than it can be formed into stars (e.g. see Fiore et al. 2017; Harrison et al. 2018). However, in the majority of observations, there are considerable uncertainties in these calculations due to uncertain spatial extents and the many assumptions that have to be considered to convert emission-line luminosities and velocities into mass outflow rates (e.g. Husemann et al. 2016; Karouzos, Woo & Bae 2016; Villar-Martín et al. 2016; Harrison et al. 2018; Rose et al. 2018; Davies et al. 2020a). On the other hand, measurements can be more accurate for more nearby sources (e.g. Baron et al. 2018; Revalski et al. 2018; Venturi et al. 2018; Fluetsch et al. 2019; Perna et al. 2020) and star formation has been detected *inside* outflows in some local AGN host galaxies, which may be a form of 'positive' feedback (Maiolino et al. 2017; Gallagher et al. 2019; Perna et al. 2020). However, samples of nearby sources typically lack the most powerful AGN, which are more common at high redshift (i.e. $z \gtrsim 1$) and are thought to be most important for influencing galaxy evolution (e.g. McCarthy et al. 2011).

At high redshift, observational evidence for a direct impact by AGN on star formation is particularly scarce. Indirect evidence may have been found in some AGN host galaxies with depleted molecular gas reservoirs; however, there are contradictory claims on this topic in the literature (e.g. Kakkad et al. 2017; Perna et al. 2018; Kirkpatrick et al. 2019; Fogasy et al. 2020). A potentially powerful approach to determine the impact of AGN-driven outflows, which has been applied to high-redshift AGN studies, has been to use integral field units (IFUs) to map narrow Hα emission to trace star formation and to map [O III] emission to trace AGN outflows. Most relevant for this work are the studies of four high-redshift AGN (presented in Cano-Díaz et al. 2012; Cresci et al. 2015b; Carniani et al. 2016) where it was suggested that there was no star formation at the location of the [O III] outflows and potentially increased star formation along the edges the outflows (see Vayner et al. 2017, for similar conclusions based on a $z = 1.4$ radio-loud quasar).

In Scholtz et al. (2020), we demonstrated some of the challenges in interpreting the aforementioned results of suppressed Hα at the location of [O III] outflows. For example, although narrow Hα emission can be used as star formation tracer, (e.g. Hao et al.

2011; Murphy et al. 2011), it is sensitive to dust obscuration and can be contaminated by AGN photoionization. Indeed, most of the star formation in high-redshift galaxies is obscured (Madau et al. 1996; Casey, Narayanan & Cooray 2014; Whitaker et al. 2014), and although obscuration corrections can help (Alaghband-Zadeh et al. 2016), sometimes the Hα emission can be *completely* hidden (e.g. Hodge et al. 2016; Chen et al. 2017, 2020). This dust absorbed emission is re-radiated at far-infrared (FIR; 8–1000 µm) wavelengths and, consequently, the FIR emission is sensitive to ongoing *obscured* star formation (for reviews see Kennicutt & Evans 2012; Calzetti 2013). Importantly for this work, high-redshift AGN and quasar host galaxies have been shown to host significant levels of star formation obscured by dust (e.g. Whitaker et al. 2012; Burgarella et al. 2013; Stanley et al. 2015, 2018).

Using additional ALMA continuum observations, Scholtz et al. (2020) re-analysed the source from Cresci et al. (2015b) with the addition of seven other moderate luminosity X-ray AGN at $z = 1.5$–2.5 ($L_X = 10^{43}$–$10^{45.5}$ erg s^{-1}). We found no direct evidence for [O III]-traced outflows suppressing or enhancing star formation. None the less, the targets in that work were moderate luminosity AGN (i.e. $L_{bol} = 10^{44}$–$10^{46.5}$ erg s^{-1}, assuming an X-ray to bolometric conversion factor of 10) and do not represent the most powerful sources, or those with the most extreme outflows. Therefore, in this work we perform similar analyses, i.e. combining ALMA measurements of the rest-frame FIR emission with IFU data, on the very powerful $z \sim 2.4$ quasars (i.e. $L_{bol} \sim 10^{47.5}$ erg s^{-1}) presented in Cano-Díaz et al. (2012) and Carniani et al. (2016). These objects were pre-selected to be bolometrically luminous and host high velocity [O III] outflows. These studies reported cavities in narrow Hα emission, which they associated with star formation, at the same spatial location of the extreme [O III] outflows, interpreting these results as evidence of negative AGN feedback in the location of the outflow and positive feedback on the edges of the outflow.

In Section 2, we describe our targets and the observations used in our study; Section 3 describes the data analyses of the ALMA and IFU observations, including spectral fitting and constructing FIR, narrow Hα emission, and outflow maps. In Section 4, we present and discuss our results, and in Section 5 we draw our conclusions. In all of our analyses, we adopt the cosmological parameters of $H_0 = 67.3$ km s^{-1}, $\Omega_M = 0.3$, and $\Omega_\Lambda = 0.7$ (Planck Collaboration XVI 2014) and assume a Chabrier (2003) initial mass function. We publish all the scripts for the data analyses here.

2 TARGET DESCRIPTION AND DATA

The primary objective of this work is a study of three quasars in which earlier studies have claimed that AGN-driven outflows suppress *in situ* host galaxy star formation. We use new ALMA band 7 observations to obtain FIR continuum images that are compared to the distribution of narrow Hα and [O III] emission derived from archival VLT/SINFONI observations. In Section 2.1, we describe the selection of our sample, in Sections 2.2 and 2.3 we describe the ALMA and IFU data we used in the analyses.

2.1 Target description

We selected three $z \sim 2.5$ type 1 quasars for this work: 2QZJ002830.4-2817 from Cano-Díaz et al. (2012) and; LBQS0109+0213 and HB89 0329-385 from Carniani et al. (2016). We note for the latter two objects the original [O III] analyses were presented in Carniani et al. (2015). We will refer to these objects in this work as 2QZJ00, LBQS01, and HB8903, respectively.

Table 1. A table of the basic properties of our quasar sample.

(1) ID	(2) Full name	(3) RA (optical)	(4) Dec. (optical)	(5) z	(6) $\log_{10}$ L_{Bol}/ergs s^{-1}	(7) SFR(FIR) (M$_\odot$ yr^{-1})	(8) $\log_{10}$ (M_{BH}/M$_\odot$)	(9) Original work	(10) IFU K-band exposure time (ks)	(11) IFU H-band exposure time (ks)
HB8903	HB89 0329−385	52.776542	− 38.401389	2.445	47.5	<59	9.9 ± 0.3	(b)	14.4	12.6
LBQS01	LBQS0109+0213	18.070417	2.496389	2.352	47.5	69^{+170}_{-31}	10.0 ± 0.3	(b)	14.4	14.4
2QZJ00	2QZJ002830.4-281706	7.126833	− 28.284667	2.401	47.3	56^{+196}_{-25}	10.1 ± 0.3	(a)	2.4	12.6

Notes. (1) Object name used in this work; (2) Object ID from Cano-Díaz et al. (2012), Carniani et al. (2015); (3,4) Optical coordinates of the objects; (5) Redshift measured from the peak of the narrow emission lines (see Section 3.3.1); (6) Bolometric luminosity from Shemmer et al. (2004); (7) Star formation rates derived from total FIR emission estimated in Section 3.2; (8) Black hole masses compiled from Carniani et al. (2015); (9) Original paper analysing the VLT/SINFONI data; (10) On-source exposure time in the IFU K band (H α) observations. (10) On-source exposure time in the IFU H-band ([O III]) observations.
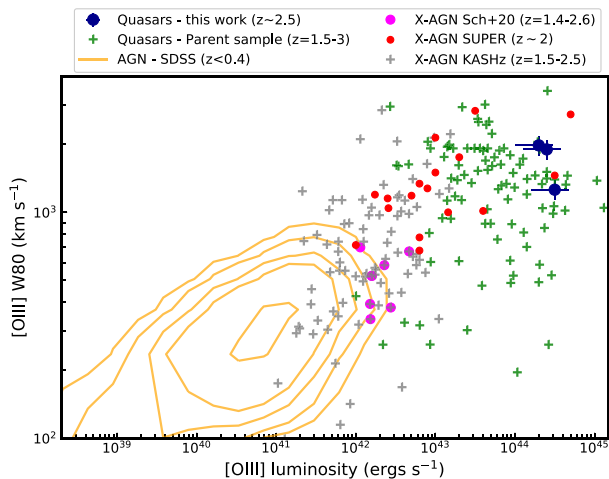(a) Cano-Díaz et al. (2012); (b) Carniani et al. (2016).

Figure 1. Plot of [O III] emission-line width (W80) versus [O III] luminosity. We compare the quasars in this study (the blue circles) with quasars and AGN populations from the following works: the parent sample of these quasars (the green crosses; Shemmer et al. 2004 and Netzer et al. 2004), spectroscopically identified $z < 0.4$ AGN from Mullaney et al. (2013; the orange contours), X-ray AGN from the KASHz survey (Harrison et al. 2016a, the grey crosses, $z = 1.2$–2.5), Type-1 X-ray AGN from the SUPER survey (the red circles, Kakkad et al. 2020), and the X-ray AGN from Scholtz et al. (2020; the magenta circles, $z = 1.4$–2.6). The three quasars studied here represent the most extreme objects in terms of bolometric power and [O III] velocities.

Originally, 2QZJ00, LBQS01, and HB8903 sources were selected as quasars with large [O III] equivalent widths (>10 Å in the rest frame) and bright in H band (<16.5 mag) from a sample of Netzer et al. (2004) and Shemmer et al. (2004; for more information see Carniani et al. 2015). These selection criteria were designed to select the most bolometrically luminous quasars during the peak epoch of galaxy and black hole growth (e.g. Madau & Dickinson 2014) that could easily have their [O III] kinematics mapped with an IFU. Furthermore, the high equivalent width [O III] lines can be easily de-blended from the emission associated with the broad line region (BLR; H β and Fe II emission; see Section 3.3.1).

We compiled the black hole masses and bolometric luminosities from Carniani et al. (2015). The black hole masses are in the range of $10^{9.9}$−$10^{10.1}$ M$_\odot$, with bolometric luminosities of $10^{47.3}$–$10^{47.5}$ erg s^{-1}, placing them at the extreme end of the quasar population (these values are discussed further in Section 4.5). The objects' names, sky coordinates, redshifts, black hole masses, and bolometric luminosities are summarized in Table 1.

Fig. 1 places our targets within the context of the overall AGN and quasar population in terms of their [O III] luminosities and [O III] line

widths (W80; velocity width containing 80 per cent of the total flux; measured in Section 3.3). We compare our sources with: the parent sample of 104 $z = 1.5$–3 quasars from Shemmer et al. (2004) and Netzer et al. (2004); the ≈24 000 $z < 0.4$ spectroscopically selected AGN from Mullaney et al. (2013); the 86 moderate luminosity X-ray AGN with IFU observations from the KMOS Survey at High-z (KASHz; Harrison et al. 2016a, and Harrison et al., in preparation), and the 18 type-1 X-ray AGN with IFU observations from the SINFONI Survey for Unveiling the Physics and Effect of Radiative feedback (SUPER; Circosta et al. 2018; Kakkad et al. 2020).[1] We also highlight the moderate luminosity X-ray AGN from Scholtz et al. (2020), where we performed a similar experiment to this one, combining ALMA data and IFU data. We note that the sources from that study were less extreme in both luminosity and [O III] emission-line width than the three targets presented here. Indeed, the three quasars in our sample have a [O III] luminosity ∼2 × 10$^{44.3}$ erg s^{-1}, a factor of ∼100 larger than a typical AGN population at $z = 1$–2.5 (Harrison et al. 2016a; Scholtz et al. 2020) and have extreme [O III] W80 values of 1260–1980 km s^{-1}.

2.2 ALMA observations and imaging

To map the rest-frame FIR emission (i.e. ≈250 μm) for our quasar host galaxies, we use ALMA band 7 data (870 μm, PI: Harrison, programme ID 2017.1.00112.S) with a native resolution of ∼0.3 arcsec and a maximum recoverable scales of ∼4.3 arcsec. The observations were performed using 45–49 antennas with a baselines range of 15–800 μm. We discuss the origin of this emission in Section 3.2.

We calibrated all the data and created the measuring sets using standard ALMA scripts using a version of Common Astronomy Software Application (CASA) applicable to the Cycle of the observations (Cycle 5; CASA v5.1.2). We performed additional checks (i.e. checking the flags, phase diagrams) to see if all calibrations (such as phase corrections) and the pipeline flagging of bad antennas pairs worked correctly and checked that none of the spectral windows used to create the continuum image contains any visible strong emission lines.

Since the ALMA band 7 observations were performed at a higher resolution than the IFU observations (0.3 arcsec compared to ∼0.5–0.6 arcsec; see Section 2.3), we chose natural weighting for the imaging of the ALMA data. This increases sensitivity while decreasing the resolution. The final images had a resolution of

---

[1]For QSOs from Shemmer et al. (2004), Netzer et al. (2004), and Mullaney et al. (2013), we used reported emission-line profile parameters (FWHM of both Gaussian components and their velocity offset) to recalculate the W80 values.
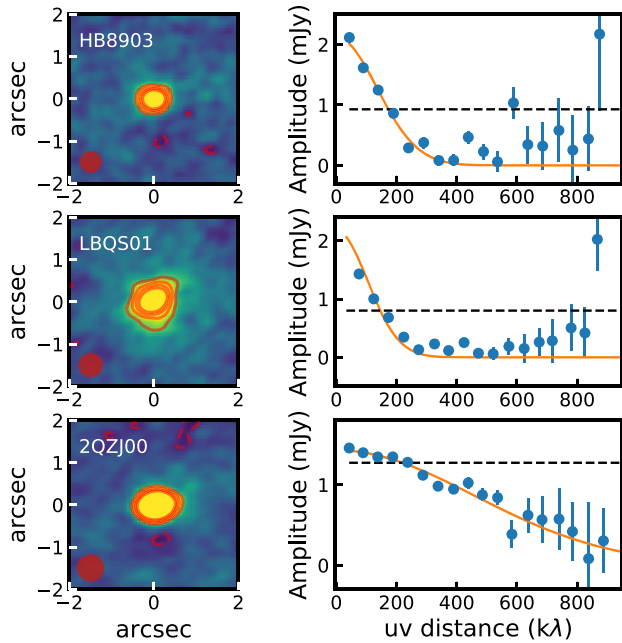
Figure 2. Summary of our analyses on the ALMA data. Left column: ALMA band 7 continuum images mapping rest-frame FIR emission. The red solid contours indicate 2σ, 3σ, 4σ, and 5σ levels of the data, while the red-dashed contours show -1σ and -2σ levels of the data. The red-shaded ellipses represent the synthesized beams of the observations. Right column: The *uv* amplitude versus *uv* distance binned per 50kλ, after subtracting any companion sources in the field. The orange solid and black-dashed curves show resolved and unresolved model fits, respectively. In all cases, the rest-frame FIR emission is resolved on 0.18–0.7 arcsec (i.e. $\approx$1.5–5.5 kpc) scales.

$\sim$0.5 arcsec, enabling a resolution-matched comparison to the IFU data. The dirty images were consequently cleaned down to 3σ by estimating the noise (root mean square; RMS) in the dirty maps. We put cleaning boxes around our primary science targets and any visible source in the image. The final RMS of the maps of 2QZJ00, LBQS01, and HB8903 is 0.05, 0.06, and 0.10 mJy beam^{-1}, respectively. This was calculated by masking any sources in the field and calculating the RMS in the primary beam. The sources are all significantly detected with peak signal-to-noise ratios (SNRs) of 28–36. We show the ALMA band 7 continuum maps in Fig. 2 and tabulate the properties of the images in Table 2.

The targets in our study were also part of an ALMA follow-up programme using band 3 observations ($\lambda \sim 3$ mm) to search for CO(3–2) emission lines (Carniani et al. 2017). The corresponding 3 mm continuum measurements in these data provide a valuable additional data point for assessing the contamination to the ALMA band 7 data point from the radio synchrotron emission during our SED analyses in Section 3.2. These observations were taken as part of programme 2013.0.00965.S and 2015.1.00407.S with a maximum baseline of 1.5 km. The data were calibrated using CASA software (version 4.5). Similar to our band 7 observations, we used natural weighting to maximize the sensitivity of our final images; however, we only select spectral windows without detected emission lines. The final resolution of our images were $\sim$0.6 arcsec with a sensitivity of 12–18 μJy beam^{-1}. The targets were detected with peak SNRs of 11–350. We use the 3 mm continuum photometry in Section 3.2. For both bands 3 and 7 data, we assumed conservative flux calibration errors of 10 per cent.

2.3 IFU data

Our targets were observed with the VLT/SINFONI integral field spectrograph, in the *K* band and *H* band to map the Hα and [O III] emission lines, respectively. The Hα IFU data were first published in Cano-Díaz et al. (2012; 2QZJ00)[2] and Carniani et al. (2016; LBQS01 and HB8903) and were observed through ESO programmes ID 077.B-0218(A) and 091.A-0261(A). The *H*-band data we use were first presented in Carniani et al. (2015) and were observed through ESO programme ID 086.B-0579(A). We note that initial results from shorter exposure *H*-band VLT/SINFONI data were presented earlier in Cano-Díaz et al. (2012).

Most of the observations were performed using the 8×8 arcsec field of view that is divided into 32 slices of width 0.25 arcsec with a pixel scale of 0.125 arcsec. The exception is the *K*-band observations of 2QZJ00 that were performed using the smaller field of view of 3×3 arcsec that is divided into 32 slices of width 0.10 arcsec with a pixel scale of 0.05 arcsec. All observations were performed using the seeing limited mode. SINFONI has a spectral resolution of R = 4000 and 3000 in *K* band and *H* band, respectively. We measured the width of the skylines (in the vicinity of the science emission lines), and this width was subtracted in quadrature from the observed emission line widths to account for spectral broadening. The on-source exposure time for the *K*-band data varied between 14.4 ks for LBQS01 and HB8903 and 2.4 ks for 2QZJ00. The short exposure for 2QZJ00 results in noticeably poorer quality *K*-band data (see more in Section 4.2). The on-source exposure time for the *H*-band data was 14.4 ks for LBQS01, 12.6 ks for HB8903, and 12.6 ks for 2QZJ00.

For as much consistency as possible between our work and the previous work, we used the published *K*-band cubes from Carniani et al. (2016).[3] None the less, the *K*-band and *H*-band IFU data for 2QZJ00 and the *H*-band data for HB8903 and LBQS01 used in this work were reduced following the same basic methods. Here, we briefly outline the procedure. The IFU data reduction was carried out using the standard techniques within ESO Recipe Execution Tool (Freudling et al. 2013). The individual exposures were stacked on the centroids determined from white-light images from the datacubes. The flux calibration solutions were derived using the IRAF routines STANDARD, SENSFUNC, and CALIBRATE on the standard stars, which were observed on the same night as the science observations.[4]

Following Scholtz et al. (2020), we use the spatial profile of the unresolved Hα and Hβ BLRs (see Appendix B.2) as a measure of the point spread function (PSF) in each cube, since it is a measure directly from the observations (i.e. this method is preferred to using a non-simultaneously observed star observation). The final full width at half-maximum (FWHM) of the PSF measured from the spatial profile of the unresolved BLR is 0.4 arcsec for 2QZJ00 and 0.6 arcsec for the LBQS01 and HB8903, for the *K*-band observations. For the *H*-band data, the FWHM of the PSF is $\sim$0.5 arcsec, for all targets, consistent with reports by the original studies using the same data.

---

[2] We note that Williams et al. (2017) presented adaptive optics assisted SINFONI IFU data for 2QZJ00. However, their study focuses on the properties of the broad line region and they find that the star-forming regions and diffuse spatially resolved [O III] outflows are not detected in these data. We therefore focus on the data presented in Cano-Díaz et al. (2012) for our re-assessment of the relationship between outflows and star formation in this quasar.

[3] Available to download at http://vizier.u-strasbg.fr/viz-bin/VizieR?-source =J/A+A/591/A28.

[4] All our reduced data cube are available here.

Table 2. A table of the basic rest-frame FIR emission (i.e. the ALMA band 7 data) properties of our quasar sample.

(1) ID	(2) FIR FWHM (`UVMultiFit`) (kpc)	(3) Flux FIR (`UVMultiFit`) (mJy)	(4) FIR FWHM (uv) (kpc)	(5) Flux FIR (uv) (mJy)	(6) FIR FWHM `IMFit` (kpc)	(7) Flux FIR `IMFit` (mJy)	(8) FIR SNR	(9) RMS (mJy)	(10) FIR beam (arcsec)
HB8903	3.7 ± 0.5	1.486 ± 0.079	4.5 ± 0.7	1.99 ± 0.24	3.7 ± 0.5	1.486 ± 0.079	28	0.10	0.48×0.39
LBQS01	5.5 ± 0.3	$2.00 \pm 0.16.$	5.4 ± 0.7	1.9 ± 0.13	4.5 ± 0.7	2.00 ± 0.16	29	0.06	0.54×0.40
2QZJ00	1.7 ± 0.3	1.1 ± 0.04	3.0 ± 0.5	1.21 ± 0.15	2.1 ± 0.3	1.092 ± 0.027	36	0.05	0.61×0.45

Notes. (1) Object ID in this paper0, (2) the FWHM radii of the rest-frame FIR emission derived using `UVMultiFit` (see Section 3.1), (3) flux density of the rest-frame FIR continuum measured using `UVMultiFit`, (4) the FWHM radii of the rest-frame FIR emission derived in the *uv*-plane (see Section 3.1), (5) flux density of the rest-frame FIR continuum measured in the *uv* plane, (6) the FWHM radii of the rest-frame FIR emission derived in the image-plane (see Section 3.1), (7) flux density of the rest-frame FIR continuum measured in the image-plane, (8) SNR of the peak rest-frame FIR continuum measured from the maps, (9) RMS of the rest-frame FIR maps, and (10) beam size of the final rest-frame FIR maps.

2.4 Astrometric alignment

The goal of this study is to compare the location of the rest-frame FIR emission traced by ALMA band 7 with the rest-frame optical emission lines traced by the VLT/SINFONI observations, and hence, we need to accurately align the two astrometric frames. The nature of interferometric observations requires accurate astrometry of the targets to reliably calculate the phase differences from each of the antennas. The absolute astrometric accuracy of ALMA depends on the baseline and frequency of the observations. For our set-up of baseline 800 m and 350 GHz, the accuracy of the astrometric frame is ≈20–30 mas (ALMA Cycle 7 Technical Handbook[5]).

For the astrometric calibration of the IFU data, we follow the basic procedure described in Scholtz et al. (2020; also similar to Carniani et al. 2017, who also align ALMA and SINFONI IFU data). For our reference astrometry in this study, we use *Gaia* observations. Although there is a lack of sufficiently high spatial resolution *near-infrared* (NIR) imaging (see Section 3.2) of our targets, the continuum emission is dominated by the point source quasar emission across all optical-NIR wavelengths. Therefore, we can benefit from using the high-quality imaging available from *Gaia* to align our NIR cubes. Since our sources are sufficiently bright (*H*-band magnitude <16.5) they are easily detected in *Gaia* Data Release 2 (Gaia Collaboration 2018) data set.

To determine the central position of the quasar in the data cubes, we collapse the cubes along the spectral channels to create a white-light (continuum) image (i.e. by excluding wavelengths contaminated by emission lines). We then proceeded with fitting a simple 2D Gaussian model to the resulting continuum image. The final RA and Dec. of the central continuum positions are then determined from the corresponding *Gaia* positions. The NIR continuum is very bright in our data cubes, and the uncertainties on the final position are ∼0.1 arcsec corresponding to ∼1 pixel (see Scholtz et al. 2020, for more discussion). This astrometric alignment is sufficiently accurate for the largely qualitative conclusions in this work that compares the location of the [O III], H α, and rest-frame FIR emission (Section 4.3).

3 ANALYSES

In this study, we investigate three powerful quasars with extreme [O III] emission-line widths (see Fig. 1), which have previously been presented in the literature to have cavities in the narrow H α emission at the location of [O III] outflows (Cano-Díaz et al. 2012; Carniani et al. 2016). Specifically, we study the origin and spatial distribution

of rest-frame FIR emission and re-assess the origin and distribution of the narrow H α and [O III] outflows. In this section, we present the data analyses of the ALMA data in Section 3.1 and assess the origin of the rest-frame FIR emission in Section 3.2. In Section 3.3, we present our analyses of the *H*-band and *K*-band VLT/SINFONI data.

3.1 ALMA data analyses

In this section, we describe how we measure the flux densities and sizes of the rest-frame FIR emission traced by the ALMA band 7 observations. We note that we use the rest-frame FIR flux densities to assist in establishing the origin of this emission in Section 3.2. Following the approaches described in Scholtz et al. (2020), we measure these quantities in both the image- and the *uv*-plane.

To measure the sizes and fluxes of the ALMA band 7 emission in the image plane, we used the CASA IMFIT routine to fit a single elliptical Gaussian model, convolved with the synthesized beam, to the images shown in the left column of Fig. 2. We used these models to measure the flux densities and the sizes of FIR continuum. To do the *uv*-plane fitting, we use UVMultiFit (Martí-Vidal et al. 2014), which simultaneously fits multiple objects in the field thus allowing us to take into account the background sources that contaminate the visibilities in the measurement sets. Using IMFIT on the images, we found that the primary sources and the background sources (one per field) are all resolved. Therefore, we fit all sources with a Gaussian profile, and we used the IMFIT results as the initial guesses on the parameters.

To visualize the visibilities, we investigated how the amplitude varies as a function of *uv*-distance. To do this, we first subtracted the background sources from the visibility data by using the results from the UVMultiFit fitting process described above. Using fixvis, we then phase centred the data, now with the background sources removed, to the targets' positions. For each target, we extracted the visibility amplitudes from the measurement sets, binning the visibilities in bins of 50kλ. These are presented right column of Fig. 2. We fitted these amplitudes as a function of *uv* distance with two different functions, a constant, to represent an unresolved source (e.g. Rohlfs & Wilson 1996), and a half Gaussian model centred on 0, to represent a resolved source with a Gaussian morphology (see curves in Fig. 2). For each fit, we calculated the Bayesian information criterion (BIC).[6] The ΔBIC values between the point source and

---

[6]The Bayesian information criterion (Schwarz 1978) uses $\Delta \chi^2$ but also takes into the account the number of free parameters, by penalizing the fit for more free parameters. BIC is defined as BIC $= \Delta \chi^2 + k \log(N)$, where N is the number of data points and k is the number of free parameters.

resolve source models are 230–1700, strongly confirming that the rest-frame FIR emission is resolved in all three objects.

We obtain very good consistency in the size and flux density measurements from all our three methods across the targets (i.e. using `UVMultiFit`, `IMFIT`, and fitting the amplitudes as a function of *uv*-distance; see Table 2). We note that the flux densities are ≈1–2 mJy and although they are not formally consistent using the three different methods (because of the small fitting uncertainties), they all agree within 3–22 per cent, which is sufficient for our purposes of using them to infer SFRs and the dominant physical source of the FIR emission (where systematics dominate the uncertainties; see Section 3.2). Furthermore the sizes across all methods yield results of FWHM ≈ 2–5 kpc, and that agree within 1–2× of the uncertainties across the three methods, which is sufficient for our primary purpose of comparing to other galaxy populations at the same redshift (see Sections 3.2 and 4.3).

We use the results from the `UVMultiFit` method as the final, preferred, measurement of flux densities, and sizes. We summarize the flux densities, and sizes (from our collapsed *uv*-data fit, `IMFIT`, and `UVMUltiFit`) of the rest-frame FIR emission in Table 2.

We repeated these same sets of analyses on the ALMA band 3 data (see Section 2.2), and we also use the results from `UVMultiFit`. Our measured band 3 continuum (tracing rest-frame millimetre emission) flux densities are summarized in appendix Table D1 and they agree with those measured by Carniani et al. (2017) within the errors.

3.2 SED fitting

Here, we describe the de-composition the SEDs to establish the origin of the 870 μm emission (rest-frame FIR) from the ALMA band 7 data and to estimate SFRs. There are potentially three main sources of the FIR emission: (1) star formation heated dust, (2) AGN-heated dust, or (3) radio synchrotron emission (Dicken et al. 2008; Mullaney et al. 2011; Falkendal et al. 2019).

Our quasars were selected to be brighter than 16 mag in *H* band (Carniani et al. 2015) and, as a result, these quasars are bright enough to be detected in several all-sky surveys. We used the optical–mid-infrared photometry from 2MASS (Skrutskie et al. 2006), PanSTARRS (Chambers et al. 2016), VST-ATLAS (Shanks et al. 2015), and WISE (Mainzer et al. 2011). We also queried the 1.4 GHz radio sky surveys of FIRST (Helfand, White & Becker 2015) and NVSS (Condon et al. 1998). Additional radio photometry at 4–8 GHz was obtained from Hooper et al. (1995) and Healey et al. (2007). We include the 870 μm and 3 mm data from the ALMA bands 7 and 3 data described above. We present the compiled photometry used for our SED analyses in Table D1 in the supplementary material.

The multiwavelength SEDs of the targets were modelled using the Bayesian SED code `FortesFit` (Rosario 2019). Four SED components were used in the modelling:

(i) An AGN accretion disc with a range of spectral slopes (−1.1 to 0.75) as prescribed by the models of Slone & Netzer (2012) with a variable extinction following a Milky Way law (*B* − *V* reddening up to 1 mag).

(ii) An AGN dust emission component with a range of shapes as prescribed by the empirical templates from Mullaney et al. (2011; short-wavelength slope: −3–0.8, long-wavelength slope: −1–0.5, turnover wavelength: 20–60 microns).

(iii) Dust emission heated by star formation following the one-parameter template sequence (0–4) from Dale et al. (2014).

(iv) Radio synchrotron emission described by a broken power law with two spectral indices α_{low} at low frequencies and α_{high} at high frequencies, and a variable break frequency. In the case of HB8903, we placed a tight prior on α_{high} in the range of 1.0–2.0 and allowed the break frequency to vary in the GHz regime along with a variable α_{low} (see details below). For the other two sources, there are no constraints on the power-law slopes or break frequency, so in order to derive an upper limit, we assumed a fixed spectral slope across the radio bands ($\alpha_{\text{low}} = \alpha_{\text{high}} = 0.7$).

The 1.4 GHz and 3 mm photometry of LBQS01 and 2QZJ00 indicate a very weak potential radio synchrotron emission. For these objects, we used a tight prior on radio spectral index of ∼−0.7, which is typical for extra-galactic synchrotron-powered radio sources at low radio frequencies. However, these photometric points indicate potentially strong radio synchrotron emission in the case of HB8903. Indeed HB8903 is 'radio loud' with a radio luminosity of $L_{8.4\,\text{GHz}} = 10^{27.7}$ W Hz^{-1} (Healey et al. 2007). It was therefore necessary to further constrain the SED in the sub-mm and mm regime for this source. This exercise showed that is was necessary to use two power-law components for this target. The 3 mm continuum observed in ALMA band 3 was detected at ∼350σ, allowing us to split the data into the different spectral windows and obtain a flux density measurement in each one. Since the CO(3–2) emission was not detected in any spectral window (also see Carniani et al. 2017), we were able to use all four spectral windows. Consequently, we were able to measure the spectral index (α) to be 1.5 in this wavelength region by fitting to these four data points (see the inset plot in the top panel of Fig. 3).

Probabilistic priors were used to constrain the luminosity of the accretion disc and AGN dust emission components based on the bolometric luminosity (see Rosario et al. 2019). `FortesFit` generates full marginalized posterior distributions of FIR luminosity from star formation ($L_{\text{IR,SF}}$; over 8–1000 μm) and AGN, as well as other parameters that are not used in this work. We present the individual SEDs and the resulting fits in Fig. 3. Using these FIR luminosities (i.e. with the AGN contribution subtracted), we estimate SFRs (FIR) using the calibration from Kennicutt & Evans (2012). The SFR (FIR) values are provided in Table 1, along with their uncertainties. We note that the degeneracies of fitting the different model components are fold in our uncertainties and are showed as coloured shaded regions in Fig. 3. They were calculated as 68 per cent confidence posterior distribution functions from the fitting shown in Fig. A2 in the Supplementary material, convolved with the systematic uncertainties (0.3 dex, Kennicutt & Evans 2012) on the conversion between $L_{\text{IR,SF}}$ and SFR(FIR).

Our main concern here is to determine the dominant source of the ALMA band 7 photometric point: cold dust heated by star formation, hot dust heated by the quasar, or radio synchrotron emission from the radio jets. The SED decomposition showed that the ALMA band 7 continuum observations have a significant component tracing the cold dust heated by star formation in objects LBQS01 and 2QZJ00. Based on the SED fitting, we estimated that the AGN contamination to the ALMA band 7 continuum for LBQS01 an 2QZJ00 is 12^{+26}_{-11} and 14^{+24}_{-13} per cent, respectively, where the range accounts for 1σ confidence interval. In Appendix A, we further tested that our SED de-composition procedure performs as expected. Specifically, we show that the inferred infrared luminosity from the AGN component is correlated with the UV luminosity of the AGN but the inferred FIR luminosity from star formation is not. There is a synchrotron contribution to the band 7 ALMA photometric point of ∼3 and ∼7 per cent, for LBQS01 and 2QZJ00, respectively. In
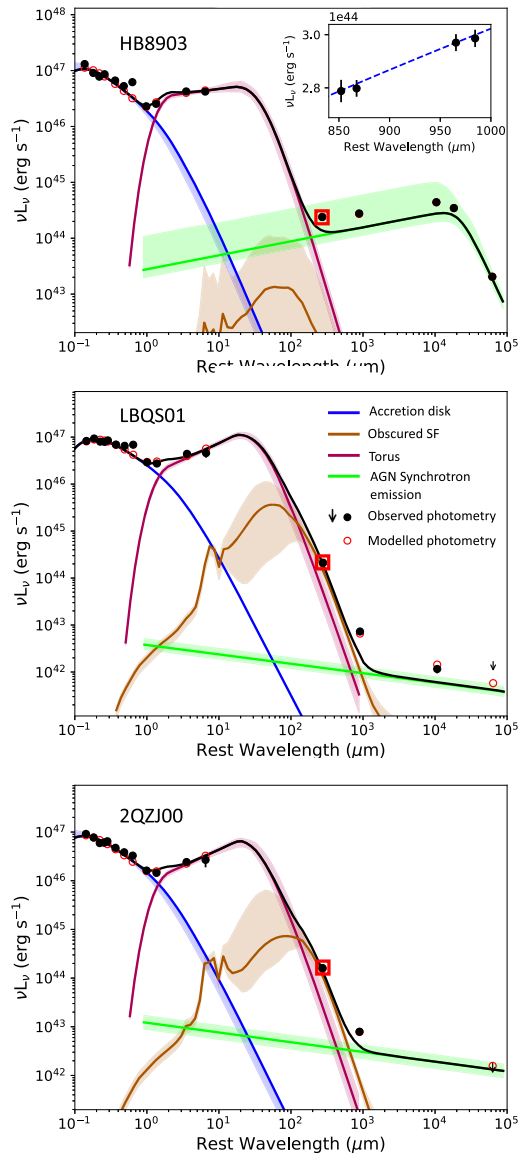
Figure 3. Results of our fitting to the optical to radio spectral energy distributions. The black, blue, red, brown, and green curves show the total fit, accretion disc, dust heated by AGN (torus), dust heated by star formation (obscured star formation), and the radio synchrotron emission, respectively. Due to nature of the SED fitting, the template visualization is sampled from a coarse grid. The black-filled points show the measured photometry, while the red empty points indicate the modelled photometry by the SED code. The ALMA band 7 photometry is highlighted by the red square. The inset figure in the top panel shows individual spectral windows of the ALMA band 3 observations. In this inset, the blue-dashed line shows the fit to these data that was used to constrain the spectral slope in the overall SED fit. The rest-frame FIR emission (250 μm) traces dust heated by star formation in LBQS01 and 2QZJ00, however, in HB8903 this emission is severally contaminated by radio synchrotron emission.

object HB8903, the ALMA band 7 continuum emission is severally contaminated by the radio synchrotron emission from the AGN (over 99 per cent). We therefore only have an upper limit (3σ) on the infrared luminosity due to star formation, and hence on the derived star formation rate.

In Fig. 4, we compare our sample in the FIR size versus FIR star formation luminosity due to star formation with other high-redshift
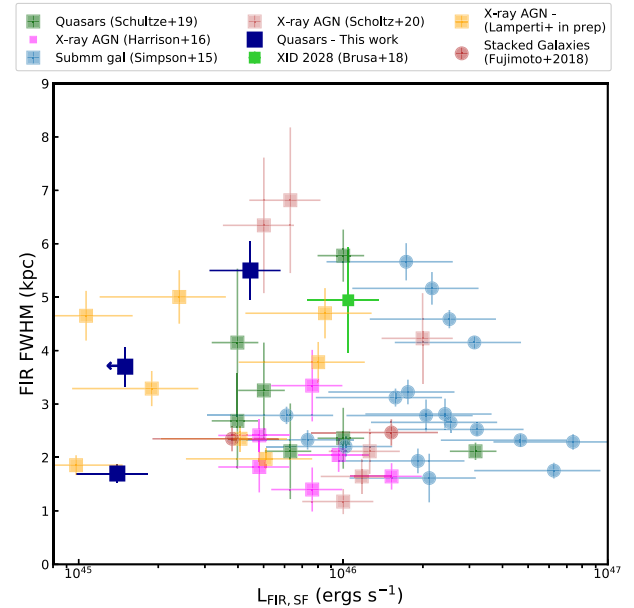

Figure 4. Plot of the total infrared luminosity due to star formation ($L_{IR,SF}$) as a function size of the FIR emission for our quasar sample (the dark blue squares), quasars from Schulze et al. (2019; dark green squares), X-ray AGN from Harrison et al. (2016b; magenta squares), Scholtz et al. (2020; the brown squares), and Lamperti et al (in preparation; the orange squares), XID 2028 (the green square, Brusa et al. 2018; Scholtz et al. 2020), submm galaxies from Simpson et al. (2015; the light blue points), and stacked $z \sim 2$ galaxies from Fujimoto et al. (2018). Our objects FIR size to luminosity ratios consistent with other quasars and star-forming galaxies.

$z \sim 2$ galaxy samples with equivalent measurements. This includes quasars, moderate luminosity AGN, and non-active galaxies. The quasars studied here fall within the scatter of these other high-redshift galaxy populations. In particular, they have FIR sizes consistent with those seen in high-redshift star-forming galaxies.

Overall, we conclude that for LBQS01 and 2QZJ00 the ALMA band 7 continuum has a significant contribution from the cold dust, whilst for HB8903 is it completely dominated by synchrotron emission.

3.3 IFU data analyses

For each of our targets, there are IFU K-band observations covering the Hα and [N II]6548,6583 emission lines and H-band observations covering the [O III]4960,5008 Å emission-line double and the Hβ emission lines (see Section 2.3). In this section, we provide information about the (a) modelling of the emission-line profiles (Section 3.3.1), (b) extraction of spectra from a grid of spatial regions across the emission-line regions (Section 3.3.2), (c) mapping of the narrow Hα emission (see Section 3.3.3), and (d) creation of [O III] velocity maps (Section 3.3.5).

3.3.1 Nuclear spectrum and emission-line modelling

We extracted an initial spectrum from the K-band and H-band cubes with the primary goal of determining the Hα+[N II] and Hβ+[O III] spectrum from the nuclear regions. We then used these to characterize the Hα and Hβ emission associated with the central quasar. To do this, we first determined the peak of the continuum emission (i.e. the central quasar location) in the IFU data cubes by
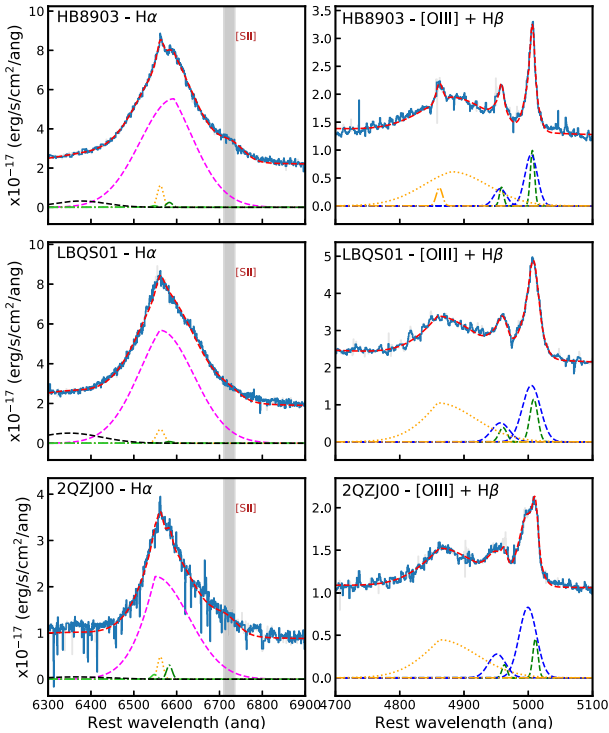
Figure 5. Hα and [N II] (left) and [O III] and Hβ (right) emission-line profiles extracted from the nuclear spectra for the three quasars in our sample. The light blue curves show the data, and the grey curves show the masked sky-line residuals. Left column: Hα spectral region. Overlaid on the Hα profiles the yellow, magenta, green, black, and red curves show the narrow Hα (dominated by NLR emission), broad line Hα, [N II], additional 'X' component and the total fit, respectively. The grey-shaded region shows the wavelength region of the [S II] emission line. Right column: [O III] emission-line profiles. The green-, dark blue, and red-dashed curves show the narrow and broad [O III] line components and the total fit, respectively. The orange-dashed and dotted lines show narrow and broad line Hβ, respectively.

collapsing the datacube in the wavelength direction, excluding any spectral channels contaminated by the emission lines or sky lines. We fitted a two-dimensional Gaussian to the continuum map to find the centre of the continuum emission. Given that the continuum emission is dominated by the emission coming from the quasar, a two-dimensional Gaussian is a sufficient model for this procedure.

For each of the targets, we extracted a spectrum with circular aperture centred on the continuum emission with a diameter of 0.5 arcsec (i.e. the approximate size of the PSF) to determine the quasar spectrum. We present these spectra in Fig. 5. This choice of aperture was chosen to be dominated by the central quasar emission whilst also maximizing the signal to noise. However, we note that our conclusions do not change if we use a different aperture.

To model the emission-line profiles observed by the IFU, each emission line was fitted with one or two Gaussian components (or modified Gaussian components; see below) with the centroid, FWHM and normalization (flux) as a free parameter. In each case, the continuum is characterized by a linear function.

To characterize the Hα emission-line profile, we simultaneously fitted the following components: (a) broad line Hα (to describe the emission from the BLR); (b) narrow Hα (which would include contributions from the AGN narrow line region [NLR], any outflows, and any contribution from star formation); and (c) [N II]6548 Å, [N II]6583 Å emission line doublet. At this point, we employ a

simple model and do not attempt to decompose any star formation, outflows, and NLR components to the overall narrow Hα emission. We will discuss this further in Section 3.3.4 and Appendix B.4. To avoid degeneracies in the fit, the central wavelength and FWHM of the narrow Hα and the [N II]6548 Å, [N II]6583 Å doublet were tied together, with rest-frame wavelengths of 6549.86, 6564.61, and 6585.27 Å, respectively. This method assumes that the Hα and [N II] originate from the same gas, a commonly used assumption in high-redshift observations (Förster Schreiber et al. 2009; Genzel et al. 2014; Harrison et al. 2016a; Förster Schreiber et al. 2018b). During the fitting, the Hα and [N II]6583 Å fluxes were free to vary but the [N II]6548 Å/[N II]6583 Å flux ratio was fixed to be 3.06 (based on the atomic transition probability; Osterbrock & Ferland 2006).

Following the approach by other studies, we modelled the broad line Hα emission, originating from the BLR, as a Gaussian component multiplied by a broken power law (Netzer et al. 2004; Nagao, Marconi & Maiolino 2006; Cresci et al. 2015b; Carniani et al. 2016; Kakkad et al. 2020; Vietri et al. 2020). This model is a good description of the asymmetrical nature of these emission-line profiles in high-luminosity sources such as our quasars. We also tested the same BLR characterization as done by the other authors, i.e. using one or two Gaussians (Cano-Díaz et al. 2012, Scholtz et al. 2020), without any changes to our conclusions on the spatial distribution of the narrow line emission.[7] In Section 4.2 and Appendix D in the Supplementary material, we discuss how more complex approaches to characterize the narrow Hα (to attempt to account for the relative contributions from an AGN narrow line region, including possible outflow components, and from star formation) do not provide robust results. Our primary approach is to model the narrow Hα emission as a single Gaussian component.

We note a small residual amount of emission above our fit over wavelengths 6300–6400 in Fig. 5 and is likely attributed to a blend of multiple weak emission lines over this region such as [O I], [S III], and [Si II]. This was treated as an additional broad and weak Gaussian component 'X' by Carniani et al. (2016). We include this component in high-SNR spectra such as the nuclear aperture and regional spectra, but we did not include in the individual spaxel spectra where the SNR is not high enough to detect it. Importantly, including this additional component, or not, does not change the properties of the narrow Hα emission which is the focus of our analyses. The [S II] emission doublet is not detected with sufficiently high SNR to be reliably modelled as both emission lines at once, and therefore we modelled this emission-line doublet as a single broad Gaussian, similar to Carniani et al. (2016). Again, this does not affect our mapping of the narrow Hα emission.

For the *H*-band IFU observations, we simultaneously fit the [O III]4959 Å, [O III]5007 Å, and Hβ emission lines, using the respective rest-frame wavelengths of 4960.3, 5008.24, and 4862.3 Å. We tied the line widths and central velocities of the [O III] lines and fixed the [O III]λ5008/[O III]λ4960 flux ratio to be 2.99 (Dimitrijević et al. 2007). Given the complexity of the [O III] line profile, and high SNRs, we found that a two Gaussian component model was a good description for each of the [O III] emission lines.

Following the same approach as for Hα, for the Hβ emission line, we fitted a narrow and a broad line component (where the latter describing the emission from the BLR). We fitted the narrow

---

[7]We note that Williams et al. (2017) characterize the broad line Hβ with both a positive and negative Gaussian component, the latter of which they attribute to an ultradense fast outflow. This is an intriguing result; however, this different approach does not affect our final conclusions

Table 3. A table of the basic properties of the Hα and [O III] emission-line profiles from the nuclear spectra.

(1) ID	(2) Narrow Hα FWHM (km s^{-1})	(3) Broad line Hα FWHM (km s^{-1})	(4) $L_{[O\,III]}$ ($\times 10^{44}$ erg s^{-1})	(5) [O III] W80 (km s^{-1})	(6) v_{broad} (km s^{-1})
HB8903	800 ± 78	7490 ± 250	3.2	1260 ± 110	-110 ± 80
LBQS01	450 ± 65	7690 ± 150	2.0	1900 ± 140	-230 ± 120
2QZJ00	620 ± 80	6590 ± 200	2.5	1980 ± 150	-580 ± 130

Note. (1) Object ID in this paper; (2) velocity FWHM of the narrow Hα component; (3) velocity FWHM of the broad line Hα component; (4) Total [O III] luminosity; (5) The W80 (velocity width containing 80% of the flux) of the [O III] emission line; (6) Velocity offset of the broad component of [O III] to the systematic redshift.

Hβ component as a single Gaussian component, while the broad line component was fitted as Gaussian profile multiplied by broken power law, similar to the broad line component of the Hα emission line, described above. In agreement with Cano-Díaz et al. (2012; also see Williams et al. 2017) and Carniani et al. (2015), we do not observe strong Fe II emission in our targets and such a component is not detected in our spatially resolved fitting (see below) and consequently does not impact upon our conclusions of the distribution of the high velocity [O III] gas.[8] Indeed, this is not surprising as the targets were pre-selected to *not* have bright Fe II emission to make the [O III] kinematic analyses easier (Carniani et al. 2015).

The emission-line profiles were fit with the models described above using the PYTHON lmfit package, excluding spectral channels that were strongly affected by the skylines. To construct a skyline residual mask, we extracted a sky spectrum from the object-free (sky only) spatial pixels in the cube and identified the strongest skyline residuals by picking any spectral pixels outside 1σ. We note that our results do not change whether we use 1σ, 3σ, and 5σ threshold for masking the sky-line residuals. These are shown as a grey spectrum in Fig. 5. We estimated the errors using a Monte Carlo approach. With this method, we added random noise (with the same RMS as the noise in the spectra) to the best-fitting solution from the initial fit and then we redid the fit. We repeated this 500 times to build a distribution of all free parameters. The median of these distributions is consistent with our original best-fitting parameters from lmfit. The final errors we quote are from the 1σ scatter of these distributions. The best-fitting parameters, and their uncertainties, for the nuclear spectra are presented in Table 3. The best-fitting models are shown on the emission-line profiles in Fig. 5.

3.3.2 Regional spectra across the emission-line regions

For a simple visual representation of the spatial variations of the emission-line profiles, and to verify the results of our more complex analyses of creating emission-line maps (derived below), we extracted spectra from nine square regions across the quasar host galaxies. These regions were defined as a 3×3 grid of 0.5×0.5 arcsec^2 (i.e. roughly equivalent to the size of the PSF of our observations). The grids were centred on the optical centre of the quasars. The entire grids sample a region of 1.5×1.5 arcsec^2 and cover most of the emission from the quasar host galaxies.

Spectral line fitting was performed on the spectra extracted from each region using the same models as described in Section 3.3.1. However, we fixed the central wavelength and line width of the Hα and Hβ broad line components to be the same as obtained from the nuclear spectrum (see Fig. 5), leaving only the flux of these components as a free parameter. This is a reasonable approach for such point source emission because only the *flux* in these broad line components will vary with angular offset, following the PSF. This approach also helps to avoid degeneracies in the fit, especially in the outer regions where the SNR of the spectra is lower.

We present two examples of our regional spectra for each of the objects in Figs 6 and 7 and for the [O III] and Hα emission-line profiles, respectively. We discuss these key spatial regions in Sections 4.1 and 4.2. The full set of [O III] regional spectra is presented in the Supplementary material in Figs C1, C2, and C3, and the full set of the Hα regional spectra is presented in the Supplementary material in Figs C4, C5, and C6.

3.3.3 Mapping narrow Hα emission

To achieve our goal of comparing the location of the rest-frame FIR emission with the emission-line gas we produced two-dimensional maps of the narrow Hα emission. That is, all of the remaining Hα emission after subtracting the broad-line region emission (see Section 3.3.1).

To map the narrow Hα emission, the most relevant previous studies (i.e. Cano-Díaz et al. 2012; Cresci et al. 2015b; Carniani et al. 2016; Scholtz et al. 2020) used two different approaches: (i) multicomponent fitting performed spaxel-by-spaxel and then visualizing the distribution of only the narrow Hα emission-line component, hereafter we call this method 'multifit'); (ii) subtracting the broad line emission and continuum emission components from the cubes first and then creating a pseudo narrow-band image of the residual emission (i.e. an image of the narrow Hα emission, as used in; hereafter we call this method 'BLR-subtraction'). In principle, these two methods should yield emission-line maps with the same flux and morphology and hence they are complementary methods to verify the integrity of the procedures. In this work we will use the results from the multifit method, however, we present the results of the BLR-subtraction method in Appendix A of the Supplementary material and the maps produced using both methods can be seen in in the Supplementary material Fig. B1. We obtain consistent conclusions with both methods.

To increase the SNR of the individual spectra during the production of the maps, we binned the spectra by performing a running median of spaxels with a radius of 0.2 arcsec. This enhances the SNR while keeping the seeing limited spatial resolution of ≈ 0.4–0.6 arcsec. This method is sufficient for our purposes of investigating the origin and morphology, on $\gtrsim 4$ kpc scales, of the narrow Hα emission (e.g.

[8]Although Carniani et al. (2015) do include a weak Fe II component for fitting the *H*-band data of LBQS01, as discussed in Section 4.1, we obtain a qualitatively consistent kinematic [O III] structure to that presented by these authors in Carniani et al. (2016; i.e. their fig. 3 compared to our Fig. 6). Therefore, our approach is sufficient for our primary purpose of mapping the high-velocity gas and for comparing to this previous work.
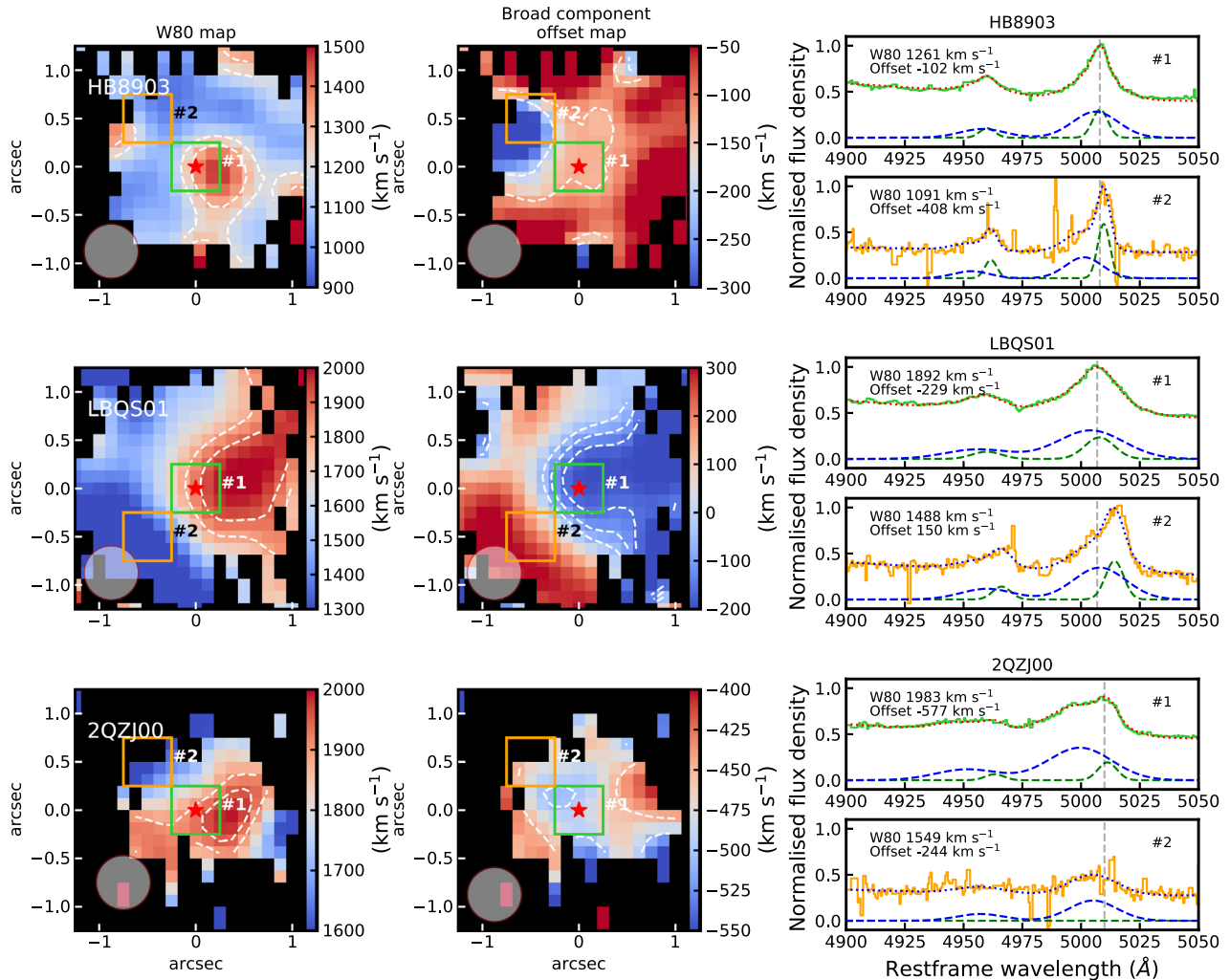
Figure 6. Summary of [O III] spectral line analyses to map AGN-driven outflows in the quasar host galaxies. Left Column: Maps of the W80 of the [O III] emission line. The white contours show the velocities of 1200 and 1300 km s^{-1} for HB8903; 1800 and 1900 km s^{-1} for LBQS01 and; 1900 and 2000 km s^{-1} for 2QZJ00. The red star shows the continuum centre (i.e. quasar position). Middle Column: Maps showing the velocity of the broad component, with respect to the systemic. The contours show the velocity offsets of −200 and −125 km s^{-1} for HB8903; −150, −100, and −50 km s^{-1} for LBQS01 and; −500 and 450 km s^{-1} for 2QZJ00. Again, the red star indicates continuum centre. The green and orange rectangles show the regions from which we extracted the emission-line profiles displayed in the right column. Right Column: Regional spectra extracted from the green (top sub-panel) and orange (bottom sub-panel) regions shown in the maps showing the [O III]4960,5008 emission-line doublet. The dark green and blue-dashed curves show the narrow and broad components of the [O III] emission line, respectively. The total fit is showed in red (top panels) and blue (bottom panels) as the dotted curves. The grey vertical dashed line represents the velocity of the quasar. We label the W80 width and velocity of the broad component for each emission-line profile for an easier comparison with the maps. The full set of regional spectra are shown in Figs C1, C2, and C3 in the Supplementary material. Extreme velocities are observed across the whole emission-line regions in all three targets.

following Cano-Díaz et al. 2012; Carniani et al. 2016, Section 4.2) and for comparing the spatial distribution of the H α emission with the [O III] outflows and FIR emission (Section 4.3). The extracted spaxel-by-spaxel emission-line profiles were fit following Section 3.3.1. The final surface brightness maps of the narrow H α component from the spatial fitting are shown in the left column of Fig. 7. In these maps, we only show values when the SNR > 3.

We performed multiple checks to verify the spaxel-by-spaxel fitting. First, we compare the total narrow H α flux in the maps to the flux from the total aperture spectra, and we find that the fluxes are consistent within uncertainties on the respective measurements. Furthermore, the distribution and flux measurements we obtain from these maps are consistent with what we observe from visually inspecting the emission-line profiles that were extracted from individual ≈0.5 × 0.5 arcsec spatial regions (Section 3.3.2; see

Fig. 7; also see Figs C4, C5, and C6 in the Supplementary material). We also checked that the surface brightness of the broad line H α emission is well fitted with a 2D Gaussian (as you would expect for the point source BLR emission following the PSF).

We performed two final tests to assess if the H α emission is centrally concentrated and if the emission is spatially resolved: (1) a curve-of-growth analyses and (2) subtracting a model PSF from the narrow H α surface brightness maps. These are described and presented in detail in Supplementary material B.2 and B.3. Both methods confirm that the narrow H α emission is centrally concentrated in all three targets. Furthermore, for LBQS01 and 2QZJ00 this emission is consistent with the PSF, i.e. it is spatially unresolved. However, we note that in LBQS01, we detect a faint region of H α emission 1 arcsec north of the quasar location. However, given that the bulk of the emission is unresolved, we still designate this target
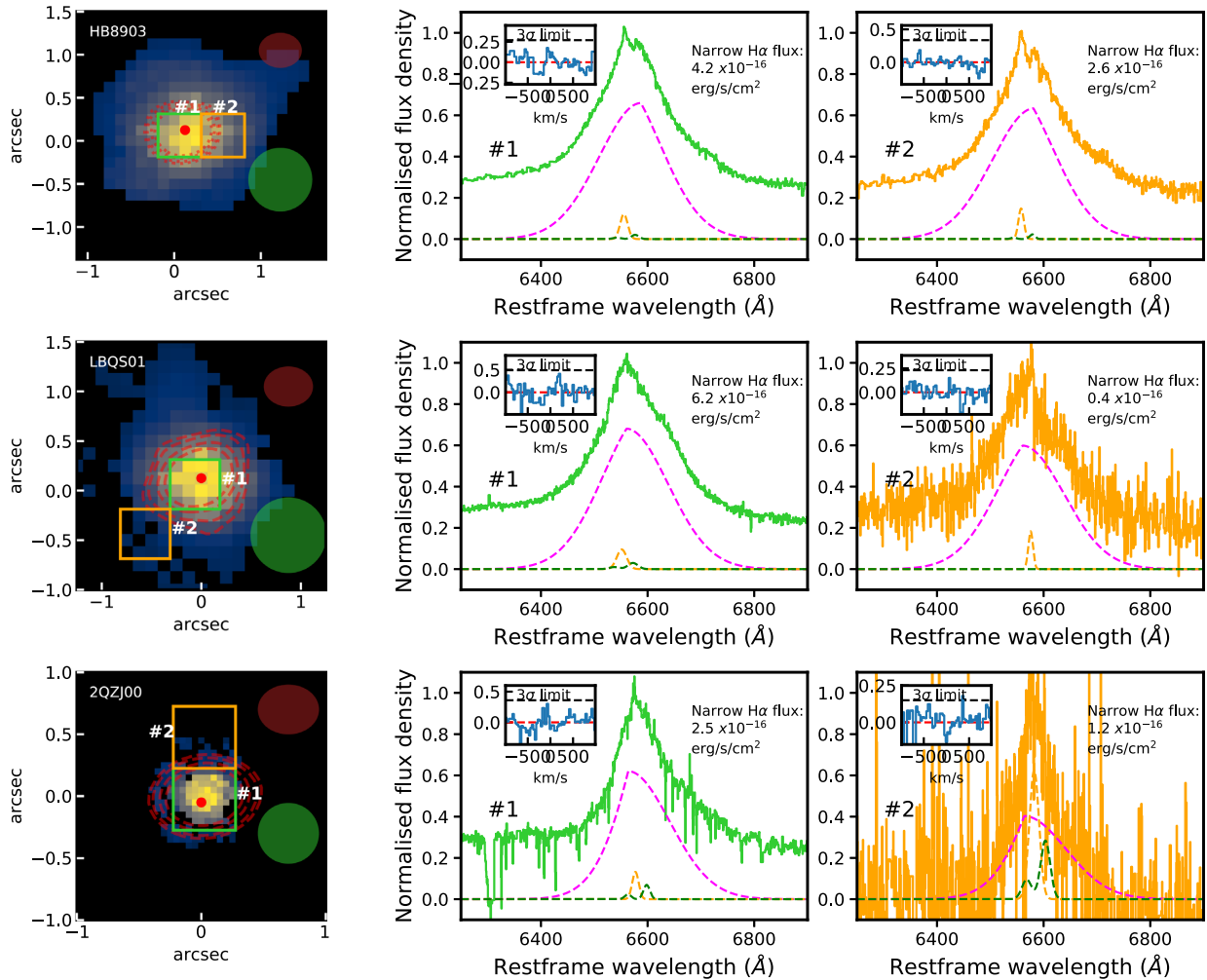
Figure 7. Left column: Narrow H α (dominated by NLR emission) surface brightness (SB) map created by simultaneously modelling all of the spaxel's spectrum components (see Section 3.3.3). The ALMA band 7 continuum data is displayed as red contours (2.5σ, 3σ, 4σ, 5σ levels). The green-shaded circles show the *K*-band PSF measured from the H α broad-line region. The light green and orange rectangles show the regions from which we extracted spectra in the middle and right columns. Middle column: Spectra extracted from the central region (the light green square). Right column: Spectra extracted from the region indicated by the orange square as indicated on the maps. We label the narrow H α flux in each subplot. Overlaid on the H α profiles, the yellow and magenta and green-dashed curves show the narrow H α (dominated by NLR emission) and broad line H α, [N II], respectively. The inset spectrum in each spectral plot are the residual spectra $-900 - 900$ km s^{-1} around the narrow H α component. We see no evidence for additional residual emission. We find that there is a strong narrow H α emission at the centres of all three quasars.

as unresolved for this work. For HB8903 these tests demonstrate that narrow H α emission is spatially resolved, but is still consistent with being centrally concentrated.

3.3.4 Interpreting the narrow H α components

As presented in Section 3.3.1, we have so-far only considered a single component to the H α emission that is not part of the BLR (i.e. the component we call 'narrow'). However, for this work it is important to establish the relative contribution from AGN NLRs, outflowing gas, and star formation to the total narrow H α flux.

Carniani et al. (2016) produced maps of residual narrow H α emission after subtracting a contribution for an AGN NLR (including any possible outflows). They considered any residual emission beyond these components to be attributed to star formation. To search for such residual emission, we created a residual cube (i.e. by subtracting the modelled spectra from the data) and inspected

it for any residual emission left by the fitting. We collapse these residual cubes along the spectral regions reported in Cano-Díaz et al. (2012) and Carniani et al. (2016) and show them in in Supplementary material Figs C4, C5, and C6. We did not detect any significant residual narrow H α emission hence forward refereed to as a narrow star formation component anywhere in the cube.

Similar to Carniani et al. (2016), we also extracted a residual ring aperture spectra of $0.5 < r < 0.8$ arcsec around the nucleus. We present these residual spectra in Fig. 8, showing ± 1000 km s^{-1} around the redshifted H α emission line. We do not detect any additional emission in these residual spectra. We further show the residuals for the individual spatial regions in Supplementary material Figs C4, C5, and C6.

We note that any residual narrow H α emission, beyond the modelled line, will be sensitive to the choice of how to model the emission line. Therefore, we investigated multiple approaches into the decomposition of the narrow H α emission line into multiple components associated with an outflow, an AGN NLR, and star
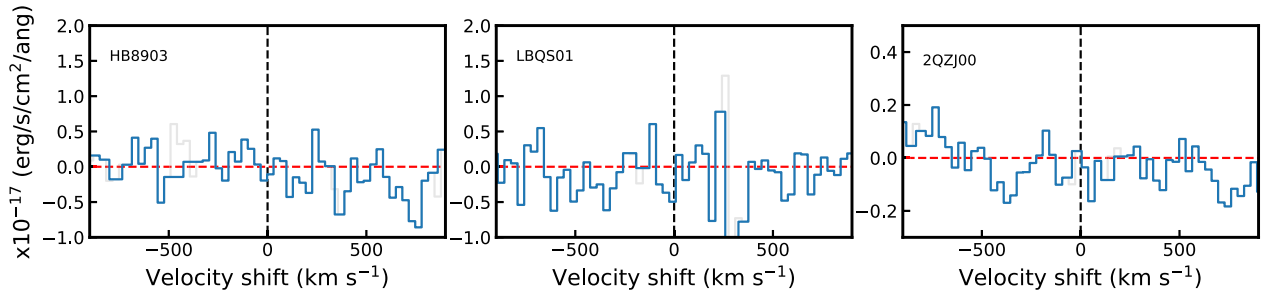
Figure 8. Residual spectra from the *K*-band Hα fitting using the 'multifit' method. The spectrum is extracted from the same ring-shaped region (0.5 < r < 0.8 arcsec) as done in Carniani et al. (2016). The black-dashed line indicates the expected location of the residual 'star formation' Hα component from Cano-Díaz et al. (2012) and Carniani et al. (2016). The red-dashed line shows the zero-point of the spectra. We do not detect any additional narrow Hα residual emission that could be associated with star formation.

formation components (see Supplementary material Section B.4). We found that fitting additional components to our spectra resulted in fits that were not statistically improved and/or they resulted in non-physical results.

Based upon all of these tests, we feel confident that our narrow Hα maps presented in Fig. 7 are a fair representation of the true morphology of the total narrow Hα emission. At the resolution of our observations, all sources are consistent with centrally concentrated narrow Hα emission, with only HB8903 being spatially resolved. However, we can only reliably identify a single component to describe the total narrow Hα emission dominated by the NLR, and we do not identify any residual narrow Hα emission that could be associated with star formation. We discuss the implications of this in Section 4.2. We stressed that despite not detecting the residual narrow 'star formation' component as previous studies, we do not claim that there is no unobscured star formation in these objects as it is most likely sub-dominant compared with the NLR Hα emission.

3.3.5 Mapping the ionized outflows traced by [O III] emission line

Following Cano-Díaz et al. (2012) and Carniani et al. (2015, 2016), we performed spaxel-by-spaxel fitting of the *H*-band IFU data to spatially map the kinematics of the [O III] emission line. The aim is to establish where the highest velocity [O III] emitting gas is located. Similar to the method used to map the narrow Hα emission, described above, we binned the spectra by the calculating the running nearby of the nearby spaxels within a radius of 0.2 arcsec, to enhance the SNR, while keeping the seeing limited spatial resolution of 0.4–0.6 arcsec.

We fitted the [O III]+Hβ spaxel spectra using the same models as for the nuclear spectra (see Section 3.3.1). However, following the same procedure that we employed for the broad line Hα (see Section 3.3.3), we fixed the line width and the central wavelength of the broad line Hβ component with only the flux as a free parameter.

The results from the spaxel-by-spaxel fitting were used to spatially map the distribution and kinematics of the [O III] emission. We focus on maps of (1) surface brightness, (2) W80, and (3) the velocity offset of the broad component from the systemic. The systematic is defined as the redshift of the narrow [O III] emission-line component in the nuclear spectra (Section 3.3.1). For these maps, we only show values when the SNRs were >3. All of these maps are presented in the Supplementary material Figs C1, C2, and C3, alongside the grids of [O III] emission-line profiles and their fits (see Section 3.3.2). The velocity maps are also shown in Fig. 6. Reassuringly, a comparison between the emission-line profiles extracted from the spatial grids and these maps demonstrates that the maps are a good description of

the data. Similar to the Hα maps, we also inspected the map of the Hβ broad line component to verify that it symmetrically fell off in flux (i.e. it was well described by a 2D Gaussian profile) to provide confidence that the fitting procedures were effective. Again, we also created the residual cube and similar to the Hα fitting, we did not detect any significant residual emission in these cubes.

For the rest of this work, we focus on the maps of W80 (i.e. the overall velocity width of the [O III] emission line) and the velocity offset (from systemic) of the broad [O III] emission-line component. This is to broadly follow the previous works of Cano-Díaz et al. (2012) and Carniani et al. (2016), respectively. Although Cano-Díaz et al. (2012) used a second moment map, instead of W80, to define the emission-line width, we verified that the spatial distribution of the high velocity width emission is the same using either definition. We present these maps, alongside example regional spectra in Fig. 6. We find extreme velocities (i.e. W80 $\gtrsim$ 1000 km s^{-1}) across the entirety of the emission-line regions in all three targets, although with spatially varying kinematic structure. We discuss the interpretation of these maps, and a comparison to the results of the previous works in Section 4.1.

4 RESULTS AND DISCUSSION

In this study, we are re-assessing the impact of powerful ionized outflows on the host galaxy star formation in three $z \sim 2.5$ quasars that have received a lot of attention in the literature because IFU data was used to provide evidence for depleted star formation at the location of [O III] outflows (Cano-Díaz et al. 2012; Carniani et al. 2016). In the previous section, we re-analysed the IFU data that was presented in this earlier work and we added new information from our ALMA band 7 observations to trace the rest-frame FIR emission. In Section 4.1, we discuss the spatial distribution of ionized outflows. In Section 4.2, we discuss the morphology and interpretation of the narrow Hα emission. In Section 4.3, we compare the location of the narrow Hα emission, rest-frame FIR emission and AGN-driven outflows. In Section 4.4, we investigate the evidence for suppressed galaxy-wide star formation. Finally, in Section 4.5 we discussed the implications of our results.

4.1 Mapping of the ionized outflows

We present our [O III] kinematic maps in Fig. 6 that were constructed using the [O III] emission-line profile models described in Section 3.3.1. There are many different definitions of 'outflow velocity' used throughout the literature (see review in Harrison et al. 2018).

Therefore, great care should be taken when interpreting outflow maps across different studies. Here, we investigate different approaches to mapping the location of outflows. We were initially motivated to reproduce the broad approaches taken in Cano-Díaz et al. (2012) and Carniani et al. (2016) who chose to plot contours of the highest [O III] emission-line widths and highest velocity offsets of a broad [O III] component, respectively (see Section 3.3.5).

The maps of [O III] W80, i.e. to characterize the total emission-line widths, are shown in the first column of Fig. 6. Based on these maps it can be seen that all three objects show extremely broad [O III] emission-line profiles *throughout* the whole emission-line regions with W80 velocities of 900–1500 km s^{-1}, 1300–2000 km s^{-1}, and 1600–2000 km s^{-1} for HB8903, LBQS01, and 2QZJ00, respectively. These extreme velocities of W80 $\gtrsim$ 1000 km s^{-1}, indicate ionized outflows are present across the full extent of the observed emission-line regions (e.g. Liu et al. 2013; Harrison et al. 2014; Kakkad et al. 2020).

In Fig. 6, we have used the white-dashed contours to highlight the regions with the *highest* [O III] emission-line widths, defined as the top ≈10 per cent of the W80 values. For HB8903, these highest velocities are found to be moderately offset by ≈0.3 arcsec (i.e. ≈2.4 kpc) to the south-east of the quasar position, for LBQS01 these are found to be ≈0.6 arcsec (i.e. ≈4.8 kpc) to the west of the quasar position and for 2QZJ00 to be ≈0.3 arcsec (i.e. ≈2.4 kpc) to the south-east of the quasar position. We find good agreement with our results and those presented in Cano-Díaz et al. (2012) and Carniani et al. (2015) for the location of these highest velocity widths. Following the approach of Carniani et al. (2016; who presented results for LBQS01 and HB8903), we also present maps of the velocity offset (from the systemic) of the broad component of the [O III] emission line in the second column of Fig. 6. Similarly as we did for W80, we show the top ≈10 per cent of (blueshifted) velocities as contours to represent the spatial location of the highest velocities. We find good agreement with Carniani et al. (2016) on the location of the highest velocity offsets.

In Fig. 6, it can already be seen that different conclusions would be drawn on the location of the highest velocities outflows if using W80 compared to broad component velocity offset. This is particularly noticeable for HB8903 where the broadest emission is towards the centre but the highest velocity offsets are to the very east of the emission-line region. Therefore, this already highlights that caution should be taken when interpreting such contours as tracing the outflow location; for example, to compare to maps of star formation tracers (see Section 4.3).

Another approach to map the ionized outflows is to look at the surface brightness distribution of the broad [O III] emission-line components, assuming that these trace outflowing gas (e.g. Rose et al. 2018; Tadhunter et al. 2018, 2019). This approach traces where the outflowing component has the greatest luminosity and, consequently, is likely to correspond to the majority of the ionized gas mass in the outflow (although using emission lines to trace outflow mass is subject to several challenges; Harrison et al. 2018). In Fig. 9, we show solid white contours of the surface brightness distribution of the broad [O III] emission-line components, derived from our spaxel-by-spaxel fitting (see Section 3.3.5). It can immediately be seen that these contours are centred around the nuclear regions. These results are in agreement with fig. 3 of Carniani et al. (2017) who show that the high velocity blue wing of the [O III] emission of LBQS01 is brightest in the nuclear regions. The same is also observed by Cano-Díaz et al. (2012) for 2QJZ00 where they find that their broad [O III] emission-line component (i.e. the one tracing the outflow) is brightest in the central regions (see their fig. A.1), even though the highest velocities
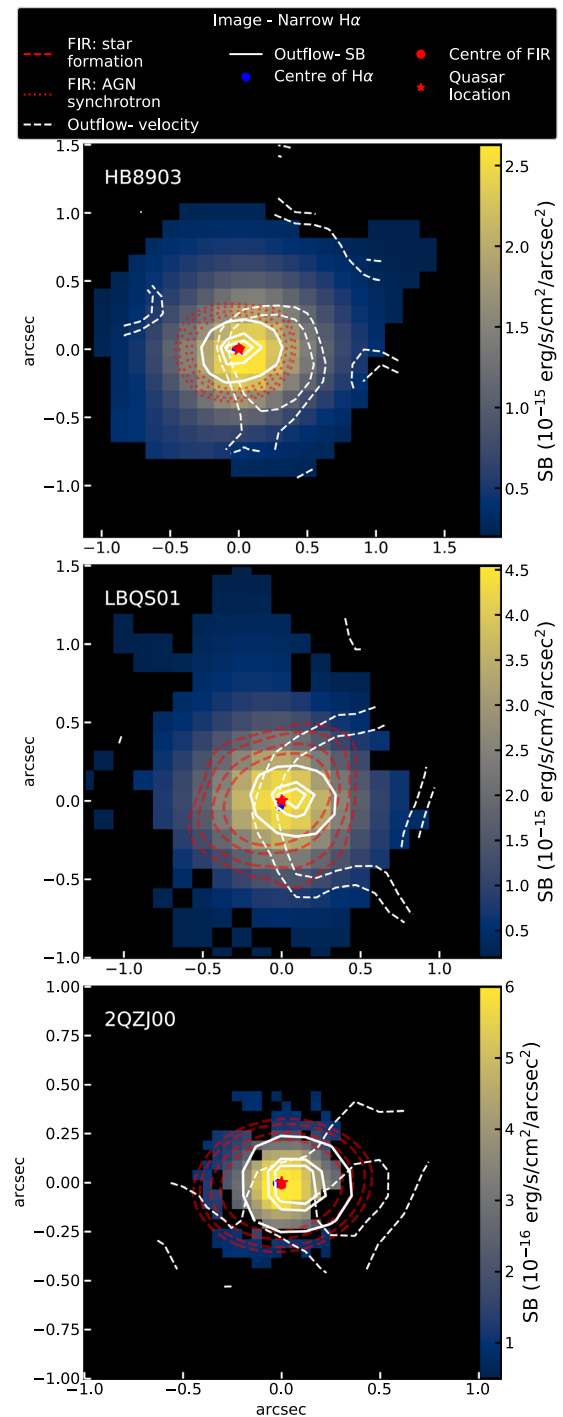

Figure 9. A comparison of the spatial distribution of FIR emission (red contours; levels of 2.5σ, 3σ, 4σ, 5σ), surface brightness of narrow Hα (dominated by NLR emission) emission (background maps; see Section 3.3.3), and AGN-driven outflows (the white contours; Section 3.3.5) for HB8903 (top); LBQS01 (middle) and; 2QZJ00 (bottom). The FIR is attributed to star formation (the red-dashed contours) for LBQS01 and 2QZJ00, and to AGN radio synchrotron for HB8903 (the red-dotted contours; Section 3.2). The white-dashed contours show [O III] W80 velocities with values of 1200 and 1300 km s^{-1} for HB8903, 1800 and 1900 km s^{-1} for LBQS01, and 1900 and 2000 km s^{-1} for 2QZJ00. The white solid contours represent the distribution of the broad [O III] 'outflow' component (levels of 0.68, 0.9, and 0.95 of the peak). The outflows peak in the centre, co-spatial with the FIR emission, but the highest velocities are found off-centre.

are located to the south. In summary, an agreement is found across our studies that the broad [O III] emission-line components peak in the centre.

In Figs 6 and 9, we have shown that different choices to define the spatial distribution of ionized outflow can give very different conclusions on the peak spatial location of these outflows. This has important ramifications for when comparing an outflow location to the spatial distribution of star formation. Fig. 9 shows that for the three quasars in this study the high velocity [O III] emission-line components are most prominent in the centre (in terms of surface brightness), even though the highest velocity widths and highest velocity offsets can be off-centre. We chose to plot contours of the most extreme ≈10 per cent of velocities in Fig. 9, following the broad approach taken by the previous work on these targets (Cano-Díaz et al. 2012; Carniani et al. 2016). However, we re-iterate that high-velocity gas is found across the entirety of the emission-line regions (see maps in Fig. 6) and the high-velocity gas is not only confined to the locations inferred by these contours.

4.2 Interpretation of the narrow H α emission

Previous works on the three quasars explored in our study presented cavities in residual H α emission (i.e. after subtracting components related to the AGN: BLR+NLR), located at the same location of the highest velocities of the AGN-driven outflows. This was interpreted as evidence that outflows rapidly suppress star formation in the vicinity of the outflows and, potentially, enhancing star formation along the edges of the outflow (Cano-Díaz et al. 2012; Carniani et al. 2016). Using the analysis from Section 3.3, we re-examined the H α emission in these targets.

We created narrow H α maps, and we present these in the left column of Fig. 7. However, as discussed in Section 3.3.4, the major source of the emission in our narrow H α maps is the NLR; hence, our labelling of this emission as dominated by NLR emission. In all three cases, we see a smooth distribution of the narrow H α emission around the quasars. As discussed at length in Section 3.3.3, we performed numerous tests to establish that these maps were a fair representation of the data. We found that the emission is consistent with being centrally compact, and is only spatially resolved in the case of HB8903.

Our tests described in Section 3.3.3 showed that only HB8903 has spatially resolved narrow H α emission (see Supplementary material Appendix B.2 and B.3) and that we were unable to identify residual emission that could be associated with star formation either in the central regions or outer regions of any of the sources (see Figs 7 and 8). Indeed, the signal-to-noise ratios of the narrow H α components are low (see Fig. 7) and therefore it is extremely challenging to reliably de-compose these into three components (i.e. an outflow, an AGN narrow line region, and star formation emission). This is especially challenging for these Type 1 quasars because the broad-line H α components are so dominant and the narrow components so weak. Although possibilities explored to help with this included tying the properties of the H α emission-line profile to the [O III] emission-line profile, this still resulted in degenerate and solutions with extreme/unrealistic emission-line ratios. It is possible that such degeneracies may be the cause of the non-physical negative surface brightness values seen in the cavities of the H α emission maps used to represent the distribution of star formation in fig. 8 of Carniani et al. (2016).

We further note the challenges in confidently establishing the dominant ionization mechanism of the H α emission. Local IFU studies demonstrate it is possible to produce AGN un-contaminated maps of star formation by using emission-line ratio diagnostics to spatially decompose the contributions from star formation, shocks, and AGN to individual kinematic components when there is sufficient signal-to-noise ratios in multiple lines and with sufficient spatial resolution. However such approaches are not feasible with these data.[9]

In summary, within the limits of these data we find that it is not possible to identify H α emission that can be confidently associated with star formation and free from AGN contamination. Therefore, the surface brightness maps of the overall narrow H α emission are likely to be dominated by AGN-related processes.

4.3 Comparison of the H α, FIR continuum, and AGN-driven outflows

In Fig. 9, we compare the spatial distribution of the narrow H α (dominated by NLR emission) emission (background map) and rest-frame FIR emission (the red contours). As demonstrated in Section 3.2, the rest-frame FIR emission is tracing dust heated by star formation in LBQS01 and 2QZJ00 (indicated as the red-dashed contours in the figure), and AGN radio synchrotron emission in HB8903 (indicated as the red-dotted contours in the figure). The H α emission is most likely dominated by AGN-related processes in all three targets (see Section 4.2). The red and blue points show the location of the peak of H α and rest-frame FIR emission, while the red star indicates the location of the quasar. The rest-frame FIR emission is centrally concentrated and we find that the peaks of the H α and rest-frame FIR emission are co-spatial in all three quasars.

At least for LBQS01 and 2QZJ00, we have shown that there are significant levels of dust in the central ≈1.5–5.5 kpc (Section 3.1). This is consistent with previous ALMA studies of sub-mm and star-forming galaxies, with and without an AGN, at high redshift that show dust emission extended over a ≈1–5 kpc (e.g. Ikarashi et al. 2015; Simpson et al. 2015; Hodge et al. 2016; Spilker et al. 2016; Harrison et al. 2016b; Tadaki et al. 2017; Brusa et al. 2018; Fujimoto et al. 2018; Lang et al. 2019; Schulze et al. 2019; Chang et al. 2020; Chen et al. 2020; Scholtz et al. 2020; Lamperti et al., in preparation; see Fig. 4). Furthermore, Carniani et al. (2017) find centrally concentrated CO(3–2) emission for LBQS01, i.e. co-spatial with the rest-frame FIR emission that we trace here. This would be consistent with obscured star formation at the same location as the molecular gas reservoir. Due to the strong radio emission in HB8903, we are not able to reliably map the distribution of dust with our observations.

We find that the rest-frame FIR emission overlaps with the H α emission cavities that were presented in Cano-Díaz et al. (2012) and Carniani et al. (2016). Therefore, without reliable obscuration corrections, observed maps of H α emission are likely to miss a significant fraction of the total intrinsic emission. Along with the several other complications discussed in Section 4.2, we suggest that the narrow H α maps presented here and in Cano-Díaz et al. (2012) and Carniani et al. (2016) are not reliable for mapping the ongoing star formation in the host galaxies.

We discussed different definitions for mapping the the [O III] outflows in Section 4.1, and we present these as white contours

---

[9]We note that the adaptive optics assisted IFU observations of 2QZJ00 in Williams et al. (2017) find that the overall emission-line ratios are consistent with AGN ionization across most of the sampled regions in their data; however, they note that most extended, diffuse, and emission associated with star formation is likely to be missed due to the use of adaptive optics.
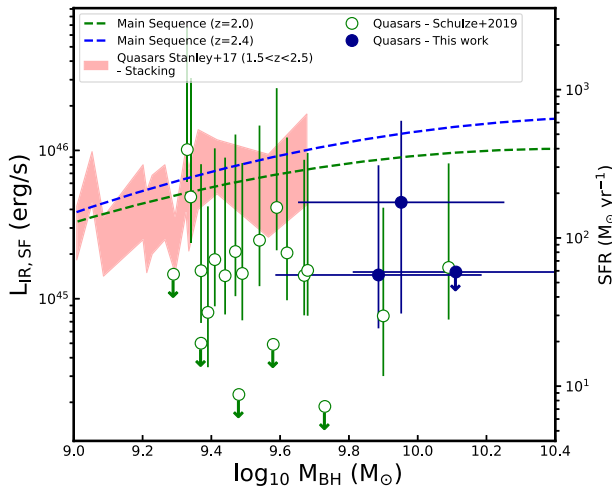
Figure 10. Plot of the total infrared luminosity due to star formation ($L_{IR,SF}$) as a function of black hole mass of the quasars. The dark blue filled and green hollow points show quasars investigated in this work and quasars from Schulze et al. (2019; $z \sim 2$), respectively. The red-shaded region shows the measured averages and 68 per cent confidence interval of quasars for redshift range of 1.5–2.5 from Stanley et al. (2017). The green- and blue-dashed lines show the expected $L_{IR,SF}$ of main-sequence galaxies (Schreiber et al. 2015; recalculated for black hole mass rather than stellar mass) for $z = 2$ and $z = 2.4$, respectively. There is some evidence that the most powerful quasars scatter to lower SFRs.

on Fig. 9, compared to the obscured star formation distribution. With either outflow definition (i.e. using velocity contours or surface brightness contours) we see no evidence that the outflows have had any significant impact on the distribution of star formation. In particular, by mapping the AGN-driven outflows in terms of the surface brightness of the broad component of the [O III] emission line, shows that the outflow is spatially located at the same location as the obscured star formation. We do see an offset between this obscured star formation and the *highest velocities* of the [O III] emission but this could be just an indication of how the outflows are escaping from the host galaxies (e.g. Gabor & Bournaud 2014, also see Section 4.5).

In summary, we find no evidence that the ionized outflows have had an instantaneous impact on the distribution of the *in situ* star formation. We discuss the limitations and implications of these conclusions in Section 4.5.

4.4 Global star formation rates of our quasars

In the previous section, we saw no evidence that star formation is disturbed at the location of the [O III] outflows in the three quasars of this study. None the less, high-velocity outflows are found across the observed emission-line regions (Fig. 6). Therefore, it is appropriate to assess if there is any evidence that the *global* (i.e. galaxy wide) SFRs of our quasar host galaxies have been suppressed, potentially by the outflows observed.

In Fig. 10, we present the SFRs (see Section 3.2) as a function of black hole masses (see Section 2.1) for the three quasars. In this figure, we compare our sample to the results of Stanley et al. (2017), who measured the mean SFR (also using FIR luminosity as their star formation tracer) of $z = 1.5$–2.5 quasars as a function of black hole mass; we show the 68 per cent confidence interval around the mean values from this study as a red-shaded region. To allow for a comparison between our quasar host galaxies and the overall star-

forming galaxy population, we also show tracks of the average SFR from Schreiber et al. (2015) for star-forming galaxies. To produce these tracks, we converted black hole mass to stellar mass following Bennert et al. 2011 and then we calculated the SFR for a given mass at both $z = 2.0$ and $z = 2.4$ following Schreiber et al. (2015). We note that our comparison to these tracks are dominated by the systematic uncertainties in SFRs and because the tracks are almost flat over the mass range of interest, the uncertainties in black hole masses or the conversions to stellar masses have no impact upon our conclusions.

In Fig. 10, it can be seen that the average SFRs of quasars, taken from Stanley et al. (2017), follow the main sequence of star-forming galaxies (in agreement with their conclusions). However, their black hole masses are limited to $< 10^{9.7} \, M_\odot$, compared to the $\approx 10^{10} \, M_\odot$ of three quasars in this study. Extrapolating the main sequence into the predicted mass range of our targets would suggest that the quasars in this study have SFRs a factor of ≈ 10 below the main sequence.

In Fig. 10, we also compare our targets to the quasars from Schulze et al. (2019). Their study observed a sample of 20 very luminous type 1 quasars at $z \sim 2$ ($\log_{10} L_{Bol} > 46.9 \, \mathrm{erg \, s^{-1}}$) with ALMA band 7, making them an ideal comparison sample to our study. To make a robust comparison between our studies, we refitted the optical to sub-mm SEDs of the Schulze et al. (2019) quasars using the FORTESFIT code described in Section 3.2. We plot the results of this re-analyses as the green hollow points in Fig. 10 where it can be seen that the quasars from Schulze et al. (2019) lie on or below the main sequence. Previous work has shown that even if the mean SFRs of AGN host galaxies follow the main sequence, the distributions can scatter to lower values (Mullaney et al. 2015; Bernhard et al. 2019). However, recent work by Grimmett et al. (2020) implies that the distribution of the more powerful AGN (such as the quasars in this study) tends towards following the same distribution as main-sequence star-forming galaxies. Broadly speaking, the powerful quasars presented here would not follow this trend as they appear to fall below the main-sequence galaxies.

Although caution should be taken when using global SFR measurements as evidence for AGN feedback, especially in the absence of specific model predictions (e.g. Harrison 2017; Scholtz et al. 2018, also see Section 4.5), based on the results presented in Fig. 10 we can not rule out that the host galaxies of the bolometrically luminous (i.e. $L_{bol} \approx 10^{47.5} \, \mathrm{ergs \, s^{-1}}$) high black hole mass (i.e. $M_{BH} \approx 10^{10} \, M_\odot$) quasars in this study are 'on the path' to becoming quenched with lower SFRs than you would expect for the black hole masses. This can also be in agreement with Carniani et al. (2017) who find that all three quasars appear to have low molecular gas content compared to main-sequence galaxies at the same redshift using observations of the CO(3–2) emission line.

4.5 Implications of our results

We have shown that there is no strong evidence that the powerful ionized outflows in the three quasars in this study have a localized '*in situ*' rapid impact on the star formation inside their host galaxies (Section 4.3). None the less, we could not rule out global SFR suppression in the host galaxies (see Carniani et al. 2016).

Our conclusions are consistent with most IFU observations (with or without adaptive optics) and inteferometric observations of high-redshift AGN that do not find strong evidence that outflows are instantaneously shutting down *in situ* star formation in the host galaxies (e.g. Scholtz et al. 2020; Davies et al. 2020b, Lamperti et al., in preparation). Our study extends this previous work to more powerful quasars with extreme outflows where the impact might be expected to be most dramatic (Fig. 1). However, we caution that our

results are only for three powerful quasars and there are samples in the literature that include sources that are even more powerful, and exhibit even more extreme outflows, than those investigated here (Zakamska et al. 2016; Bischetti et al. 2017; Perrotta et al. 2019). It would now be interesting to assess if the outflows in these systems have any impact on the *in situ* star formation.

The star formation tracer that we have been able to use in this study is FIR emission that has a mean stellar population age contribution to the emission from ≈5 Myr, up to ≈100 Myr (Kennicutt & Evans 2012). Unfortunately, we lack a reliable tracer of star formation that is *dominated* by recent star formation episodes (i.e. ≲10 Myr), which may be helpful for searching for more immediate changes in star formation. However, with current facilities, it is not clear how to reliably overcome this problem for the most powerful high-redshift quasars where the challenges of removal of AGN contamination to tracers such as H α and ultraviolet are severe, to impossible (see Section 4.2). Future studies of Type 2 quasars (as opposed to Type 1 quasars) would at least reduce the challenges of subtracting the broad line region contribution to the H α emission and the ultraviolet continuum emission associated with the accretion disc but would still suffer from many of the other challenges we outlined in Section 4.2.

When searching for observational evidence of feedback by AGN, it is also important to ask if the results are actually in conflict with specific theoretical predictions (e.g. Harrison 2017; Scholtz et al. 2018). Simulations of individual galaxies show the reality of how outflows would impact upon their host galaxies is complex. For example, simulations show that the level of any negative or positive impact on the host galaxy SFRs will depend on many factors such as: the relative orientation of an outflow (or jet) with a disc; the gas fraction and distribution of the ISM; and the luminosity of the AGN itself (e.g. Wagner, Umemura & Bicknell 2013; Pontzen et al. 2017; Zubovas & Bourne 2017; Mukherjee et al. 2018; Costa, Pakmor & Springel 2020). Furthermore, whilst simulations suggest that *some* level of rapid suppression in the SFR could be caused by AGN-driven outflows this may typically be by modest factors and only in the central regions even in the case of the powerful quasars (e.g. Gabor & Bournaud 2014; Costa et al. 2018, 2020). These simulations show complete destruction of the gas disc is extremely unlikely since outflows tend to become collimated and escape through paths of least resistance.

In agreement with the aforementioned simulations, using the greater spatial resolution possible for integral field spectroscopy and mm-inteferometry observations of local galaxies, some evidence for *modest* positive and negative feedback on *small scales* has been observed (e.g. Croft et al. 2006; Alatalo et al. 2015; Cresci et al. 2015a; Querejeta et al. 2016; Husemann et al. 2019; Rosario et al. 2019; Shin et al. 2019; Perna et al. 2020). These effects are out of reach of what can be observed with the lower (i.e. ∼2–5 kpc) resolution and sensitivity of IFU observations of high-redshift galaxies. However, even from these impressive observations of local galaxies, it is not clear if the global, long-term impact of these effects will be significant.

As discussed in Costa et al. (2020), quasars may be able to cause feedback effects without the removal of dense star-forming material. For example, through the ejection of gas from the gaseous halo, which would accelerate the decline of gas inflow from the halo. Such a process would operate on longer ∼100 Myr time-scales. Observations of the Sunyaev–Zeldovich effect have provided tantalizing evidence that quasars are effective at depositing energy into the circumgalactic environment (e.g. Crichton et al. 2016; Lacy et al. 2019). Our observations would be consistent with such a mode

of AGN feedback that has an impact on star formation over a longer time-scale, perhaps through the cumulative effect of quasar episodes (also see McCarthy et al. 2011; Zubovas & King 2012; Gabor & Bournaud 2014; Scholtz et al. 2018; Costa et al. 2020).

5 CONCLUSIONS

We have presented new high-resolution ALMA band 7 continuum observations (rest-frame λ ∼ 250 μm) of three quasars at $z \sim 2.5$ that have previously been presented as showing evidence for suppressed star formation based on cavities in the narrow H α emission at the location of the quasar-driven outflows (traced with [O III] emission; Cano-Díaz et al. 2012; Carniani et al. 2016). All three quasars are significantly detected by ALMA (SNR > 25), and we exploited these observations to trace the dust-obscured star formation. Furthermore, we re-analysed the *H*-band and *K*-band archival IFU data. Based on our analyses we find the following:

(i) **FIR emission contains a significant dust-obscured star formation component in two of the three quasars.** This result is based on (1) the observation that the FIR emission traced by ALMA band 7 observations is spatially extended on scales typical for high-redshift star-forming galaxies (i.e. ≈1.5–5.5 kpc; see Figs 2 and 4) and (b) our SED decomposition shows that the FIR emission contains a significant star formation heated dust component (∼ 86 per cent; see Section 3.2 and Fig. 3); therefore, we conclude that we can use the spatially resolved maps to trace the obscured star formation in LBQS01 and 2QZJ00, and this star formation is located in the regions of the previously reported cavities in the narrow H α emission (Fig. 9). In the third quasar (HB8903), the FIR emission is dominated by AGN synchrotron emission.

(ii) **High velocity ionized gas is found across the whole emission-line regions as traced by the [O III] emission line (W80 ≳ 1000 km s⁻¹).** This is based on our [O III] velocity maps (Fig. 6). Following the approach of the previous work, when the outflow locations are defined based on the top ≈10 per cent of emission-line velocities, they are offset by ≈2–5 kpc from the central quasar. However, based on the surface brightness distribution of the broad component of the [O III] emission line, the outflows peak in the centre (see Fig. 9). Consequently, the relative spatial distribution of an outflow and star formation is sensitive to the choice of outflow definition.

(iii) **We do not identify any H α emission that is a reliable tracer of spatially resolved star formation** despite testing a variety approaches to isolate such emission. This is because we are unable to reliably identify any residual H α emission beyond that associated with the AGN narrow line region and/or outflow in the galaxy-integrated or spatially resolved spectra (see Figs 7 and 8). Furthermore, the H α emission is only spatially resolved in one of the three targets.

(iv) **We do not observe any localized instantaneous suppression of star formation by the ionized outflows.** Specifically, we do not find any evidence for suppressed star formation co-spatial with the location of the bulk of the ionized outflows, at least for the two targets for which we have been able to trace the star formation with the ALMA data (see Fig. 9).

(v) **We cannot rule out global star formation suppression caused by the quasars.** Based on the infrared luminosities we find that the inferred galaxy-wide SFRs of the three quasars are 50–170 M⊙ yr⁻¹. Assuming a black hole to stellar mass conversion from Bennert et al. (2011), these are an order of magnitude lower than mass-matched main-sequence galaxies at the same redshift. This

could also be in agreement with the findings of Carniani et al. (2017), who reported low molecular gas content in these same objects.

Using the FIR emission as a tracer of star formation, we see no direct evidence that ionized outflows instantaneously suppress *in situ* star formation in the nuclear regions of these extreme quasars on ~4 kpc scales. Any instantaneous impact by these outflows must be subtle, occurring beyond that which can be detected within the resolution and sensitivity limits of these observations. This is consistent with Scholtz et al. (2018) that showed a good agreement between ALMA observations of X-ray AGN and the predictions from EAGLE hydrodynamical simulation. To search for more subtle effects will require deep observations with future high-resolution IFU facilities such as with VLT/ERIS, *JWST*/NIRSpec, and ELT/HARMONI. We suggest that any impact on star formation from a single outflow event must be limited. However, our results could still be consistent with a more long-term impact of the central quasars resulting in a more gradual global suppression; for example, the cumulative effect of outflow episodes could accelerate the decline of gas inflow on to the host galaxy (also see e.g. Cano-Díaz et al. 2012; Gabor & Bournaud 2014; Carniani et al. 2016; Costa et al. 2020).

ACKNOWLEDGEMENTS

DATA AVAILABILITY

The raw IFU and ALMA data are available at VLT/SINFONI and ALMA archive services. The reduced data and main analyses code underlying this article are available on GITHUB here.

REFERENCES

Alaghband-Zadeh S., Banerji M., Hewett P. C., McMahon R. G., 2016, MNRAS, 459, 999

Alatalo K. et al., 2015, ApJ, 798, 31
Alexander D. M., Hickox R. C., 2012, New Astron. Rev., 56, 93
Balmaverde B., Capetti A., 2015, A&A, 581, A76
Balmaverde B. et al., 2016, A&A, 585, A148
Baron D. et al., 2018, MNRAS, 480, 3993
Beckmann R. S. et al., 2017, MNRAS, 472, 949
Bennert V. N., Auger M. W., Treu T., Woo J.-H., Malkan M. A., 2011, ApJ, 742, 107
Bernhard E., Grimmett L. P., Mullaney J. R., Daddi E., Tadhunter C., Jin S., 2019, MNRAS, 483, L52
Bischetti M. et al., 2017, A&A, 598, A122
Brusa M. et al., 2015, MNRAS, 446, 2394
Brusa M. et al., 2018, A&A, 612, A29
Burgarella D. et al., 2013, A&A, 554, A70
Calzetti D., 2013, Star Formation Rate Indicators. Cambridge Univ. Press, Cambridge, UK, p. 419
Cano-Díaz M., Maiolino R., Marconi A., Netzer H., Shemmer O., Cresci G., 2012, A&A, 537, L8
Carniani S. et al., 2015, A&A, 580, A102
Carniani S. et al., 2016, A&A, 591, A28
Carniani S. et al., 2017, A&A, 605, A105
Casey C. M., Narayanan D., Cooray A., 2014, Phys. Rep., 541, 45
Chabrier G., 2003, PASP, 115, 763
Chambers K. C. et al., 2016, preprint (arXiv:1612.05560)
Chang Y.-Y. et al., 2020, ApJ, 888, 44
Chen C.-C. et al., 2017, ApJ, 846, 108
Chen C.-C. et al., 2020, A&A, 635, A119
Choi E., Somerville R. S., Ostriker J. P., Naab T., Hirschmann M., 2018, ApJ, 866, 91
Cicone C., Feruglio C., Maiolino R., Fiore F., Piconcelli E., Menci N., Aussel H., Sturm E., 2012, A&A, 543, A99
Cicone C. et al., 2014, A&A, 562, A21
Cicone C., Brusa M., Ramos Almeida C., Cresci G., Husemann B., Mainieri V., 2018, Nat. Astron., 2, 176
Circosta C. et al., 2018, A&A, 620, A82
Condon J. J., Cotton W. D., Greisen E. W., Yin Q. F., Perley R. A., Taylor G. B., Broderick J. J., 1998, AJ, 115, 1693
Costa T., Rosdahl J., Sijacki D., Haehnelt M. G., 2018, MNRAS, 479, 2079
Costa T., Pakmor R., Springel V., 2020, MNRAS, 497, 5229
Crain R. A. et al., 2015, MNRAS, 450, 1937
Cresci G., Maiolino R., 2018, Nat. Astron., 2, 179
Cresci G. et al., 2015a, A&A, 582, A63
Cresci G. et al., 2015b, ApJ, 799, 82
Crichton D. et al., 2016, MNRAS, 458, 1478
Croft S. et al., 2006, ApJ, 647, 1040
Dale D. A., Helou G., Magdis G. E., Armus L., Díaz-Santos T., Shi Y., 2014, ApJ, 784, 83
Davies R. et al., 2020a, MNRAS, 498, 4150
Davies R. L. et al., 2020b, ApJ, 894, 28
Di Matteo T., Springel V., Hernquist L., 2005, Nature, 433, 604
Dicken D., Tadhunter C., Morganti R., Buchanan C., Oosterloo T., Axon D., 2008, ApJ, 678, 712
Dimitrijević M. S., Popović L. Č., Kovačević J., Dačić M., Ilić D., 2007, MNRAS, 374, 1181
Dubois Y., Pichon C., Devriendt J., Silk J., Haehnelt M., Kimm T., Slyz A., 2013a, MNRAS, 428, 2885
Dubois Y., Gavazzi R., Peirani S., Silk J., 2013b, MNRAS, 433, 3297
Falkendal T. et al., 2019, A&A, 621, A27
Feruglio C. et al., 2015, A&A, 583, A99
Fiore F. et al., 2017, A&A, 601, A143
Fluetsch A. et al., 2019, MNRAS, 483, 4586
Fogasy J., Knudsen K. K., Drouart G., Lagos C. D. P., Fan L., 2020, MNRAS, 493, 3744
Förster Schreiber N. M. et al., 2009, ApJ, 706, 1364
Förster Schreiber N. M. et al., 2018a, ApJS, 238, 21
Förster Schreiber N. M. et al., 2018b, ApJS, 238, 21
Freudling W., Romaniello M., Bramich D. M., Ballester P., Forchi V., García-Dabló C. E., Moehler S., Neeser M. J., 2013, A&A, 559, A96

Fujimoto S. et al., 2018, ApJ, 861, 7

Gabor J. M., Bournaud F., 2014, MNRAS, 441, 1615

Gaia Collaboration et al., 2018, A&A, 616, A1

Gallagher R., Maiolino R., Belfiore F., Drory N., Riffel R., Riffel R. A., 2019, MNRAS, 485, 3409

Ganguly R., Brotherton M. S., 2008, ApJ, 672, 102

Genzel R. et al., 2014, ApJ, 796, 7

Grimmett L. P., Mullaney J. R., Bernhard E. P., Harrison C. M., Alexander D. M., Stanley F., Masoura V. A., Walters K., 2020, MNRAS, 495, 1392

Hao C.-N., Kennicutt R. C., Johnson B. D., Calzetti D., Dale D. A., Moustakas J., 2011, ApJ, 741, 124

Harrison C. M., 2017, Nat. Astron., 1, 0165

Harrison C. M. et al., 2012, ApJ, 760, L15

Harrison C. M., Alexander D. M., Mullaney J. R., Swinbank A. M., 2014, MNRAS, 441, 3306

Harrison C. M. et al., 2016a, MNRAS, 456, 1195

Harrison C. M. et al., 2016b, MNRAS, 457, L122

Harrison C. M., Costa T., Tadhunter C. N., Flütsch A., Kakkad D., Perna M., Vietri G., 2018, Nat. Astron., 2, 198

Healey S. E., Romani R. W., Taylor G. B., Sadler E. M., Ricci R., Murphy T., Ulvestad J. S., Winn J. N., 2007, ApJS, 171, 61

Helfand D. J., White R. L., Becker R. H., 2015, ApJ, 801, 26

Hirschmann M., Dolag K., Saro A., Bachmann L., Borgani S., Burkert A., 2014, MNRAS, 442, 2304

Hodge J. A. et al., 2016, ApJ, 833, 103

Hooper E. J., Impey C. D., Foltz C. B., Hewett P. C., 1995, ApJ, 445, 62

Husemann B., Scharwächter J., Bennert V. N., Mainieri V., Woo J.-H., Kakkad D., 2016, A&A, 594, A44

Husemann B. et al., 2019, A&A, 627, A53

Ikarashi S. et al., 2015, ApJ, 810, 133

Jarvis M. E. et al., 2019, MNRAS, 485, 2710

Kakkad D. et al., 2016, A&A, 592, A148

Kakkad D. et al., 2017, MNRAS, 468, 4205

Kakkad D. et al., 2020, A&A, 642, A147

Karouzos M., Woo J.-H., Bae H.-J., 2016, ApJ, 819, 148

Kennicutt R. C., Evans N. J., 2012, ARA&A, 50, 531

Kirkpatrick A., Sharon C., Keller E., Pope A., 2019, ApJ, 879, 41

Kormendy J., Ho L. C., 2013, ARA&A, 51, 511

Lacy M. et al., 2019, MNRAS, 483, L22

Lang P. et al., 2019, ApJ, 879, 54

Lansbury G. B., Jarvis M. E., Harrison C. M., Alexander D. M., Del Moro A., Edge A. C., Mullaney J. R., Thomson A. P., 2018, ApJ, 856, L1

Leung G. C. K. et al., 2017, ApJ, 849, 48

Liu G., Zakamska N. L., Greene J. E., Nesvadba N. P. H., Liu X., 2013, MNRAS, 436, 2576

Madau P., Dickinson M., 2014, ARA&A, 52, 415

Madau P., Ferguson H. C., Dickinson M. E., Giavalisco M., Steidel C. C., Fruchter A., 1996, MNRAS, 283, 1388

Mainzer A. et al., 2011, ApJ, 731, 53

Maiolino R. et al., 2017, Nature, 544, 202

Martí-Vidal I., Vlemmings W. H. T., Muller S., Casey S., 2014, A&A, 563, A136

McCarthy I. G., Schaye J., Bower R. G., Ponman T. J., Booth C. M., Dalla Vecchia C., Springel V., 2011, MNRAS, 412, 1965

McElroy R. E. et al., 2016, A&A, 593, L8

Merloni A., Rudnick G., Di Matteo T., 2004, MNRAS, 354, L37

Morganti R., Tadhunter C. N., Oosterloo T. A., 2005, A&A, 444, L9

Mukherjee D., Bicknell G. V., Wagner A. Y., Sutherland R. S., Silk J., 2018, MNRAS, 479, 5544

Mullaney J. R., Alexander D. M., Goulding A. D., Hickox R. C., 2011, MNRAS, 414, 1082

Mullaney J. R., Alexander D. M., Fine S., Goulding A. D., Harrison C. M., Hickox R. C., 2013, MNRAS, 433, 622

Mullaney J. R. et al., 2015, MNRAS, 453, L83

Murphy E. J., Chary R.-R., Dickinson M., Pope A., Frayer D. T., Lin L., 2011, ApJ, 732, 126

Nagao T., Marconi A., Maiolino R., 2006, A&A, 447, 157

Netzer H., Shemmer O., Maiolino R., Oliva E., Croom S., Corbett E., di Fabrizio L., 2004, ApJ, 614, 558

Osterbrock D. E., Ferland G. J., 2006, Astrophysics of Gaseous Nebulae and Active Galactic Nuclei, 2nd edn. University Science Books, Sausalito, CA

Perna M. et al., 2018, A&A, 619, A90

Perna M., Cresci G., Brusa M., Lanzuisi G., Concas A., Mainieri V., Mannucci F., Marconi A., 2019, A&A, 623, A171

Perna M. et al., 2020, A&A, 643, A139

Perrotta S., Hamann F., Zakamska N. L., Alexand roff R. M., Rupke D., Wylezalek D., 2019, MNRAS, 488, 4126

Planck Collaboration XVI, 2014, A&A, 571, A16

Pontzen A., Tremmel M., Roth N., Peiris H. V., Saintonge A., Volonteri M., Quinn T., Governato F., 2017, MNRAS, 465, 547

Querejeta M. et al., 2016, A&A, 593, A118

Ramos Almeida C., Acosta-Pulido J. A., Tadhunter C. N., González-Fernández C., Cicone C., Fernández-Torreiro M., 2019, MNRAS, 487, L18

Revalski M. et al., 2018, ApJ, 867, 88

Rohlfs K., Wilson T. L., 1996, Tools of Radio Astronomy, XVI. Springer-Verlag Berlin, Heidelberg, New York, p. 127

Rosario D. J., 2019, Astrophysics Source Code Library, record ascl:1904.011

Rosario D. J., Togi A., Burtscher L., Davies R. I., Shimizu T. T., Lutz D., 2019, ApJ, 875, L8

Rose M., Tadhunter C., Ramos Almeida C., Rodríguez Zaurín J., Santoro F., Spence R., 2018, MNRAS, 474, 128

Rupke D. S. N., Gültekin K., Veilleux S., 2017, ApJ, 850, 40

Scholtz J. et al., 2018, MNRAS, 475, 1288

Scholtz J. et al., 2020, MNRAS, 492, 3194

Schreiber C. et al., 2015, A&A, 575, A74

Schulze A. et al., 2019, MNRAS, 488, 1180

Schwarz G., 1978, Ann. Stat., 6, 461

Segers M. C., Schaye J., Bower R. G., Crain R. A., Schaller M., Theuns T., 2016, MNRAS, 461, L102

Shanks T. et al., 2015, MNRAS, 451, 4238

Shemmer O., Netzer H., Maiolino R., Oliva E., Croom S., Corbett E., di Fabrizio L., 2004, ApJ, 614, 547

Shin J., Woo J.-H., Chung A., Baek J., Cho K., Kang D., Bae H.-J., 2019, ApJ, 881, 147

Silk J., Rees M. J., 1998, A&A, 331, L1

Simpson J. M. et al., 2015, ApJ, 807, 128

Skrutskie M. F. et al., 2006, AJ, 131, 1163

Slone O., Netzer H., 2012, MNRAS, 426, 656

Soltan A., 1982, MNRAS, 200, 115

Spilker J. S. et al., 2016, ApJ, 826, 112

Stanley F., Harrison C. M., Alexander D. M., Swinbank A. M., Aird J. A., Del Moro A., Hickox R. C., Mullaney J. R., 2015, MNRAS, 453, 591

Stanley F. et al., 2017, MNRAS, 472, 2221

Stanley F., Harrison C. M., Alexander D. M., Simpson J., Knudsen K. K., Mullaney J. R., Rosario D. J., Scholtz J., 2018, MNRAS, 478, 3721

Storchi-Bergmann T., Lopes R. D. S., McGregor P. J., Riffel R. A., Beck T., Martini P., 2010, MNRAS, 402, 819

Sturm E. et al., 2011, ApJ, 733, L16

Tadaki K.-i. et al., 2017, ApJ, 834, 135

Tadhunter C. et al., 2018, MNRAS, 478, 1558

Tadhunter C., Holden L., Ramos Almeida C., Batcheldor D., 2019, MNRAS, 488, 1813

Vayner A., Wright S. A., Murray N., Armus L., Larkin J. E., Mieda E., 2017, ApJ, 851, 126

Veilleux S., Cecil G., Bland-Hawthorn J., 2005, ARA&A, 43, 769

Veilleux S. et al., 2013, ApJ, 776, 27

Veilleux S., Maiolino R., Bolatto A. D., Aalto S., 2020, A&AR, 28, 2

Venturi G. et al., 2018, A&A, 619, A74

Vietri G. et al., 2020, A&A, 644, A175

Villar-Martín M., Arribas S., Emonts B., Humphrey A., Tadhunter C., Bessiere P., Cabrera Lavers A., Ramos Almeida C., 2016, MNRAS, 460, 130

Vogelsberger M. et al., 2014, MNRAS, 444, 1518

Wagner A. Y., Umemura M., Bicknell G. V., 2013, ApJ, 763, L18
Whitaker K. E., van Dokkum P. G., Brammer G., Franx M., 2012, ApJ, 754, L29
Whitaker K. E. et al., 2014, ApJ, 795, 104
Williams R. J., Maiolino R., Krongold Y., Carniani S., Cresci G., Mannucci F., Marconi A., 2017, MNRAS, 467, 3399
Woo J.-H., Bae H.-J., Son D., Karouzos M., 2016, ApJ, 817, 108
Woo J.-H., Son D., Bae H.-J., 2017, ApJ, 839, 120
Woo J.-H., Son D., Rakshit S., 2020, ApJ, 901, 66
Wylezalek D., Zakamska N. L., 2016, MNRAS, 461, 3724
Zakamska N. L., Greene J. E., 2014, MNRAS, 442, 784
Zakamska N. L. et al., 2016, MNRAS, 459, 3144
Zubovas K., Bourne M. A., 2017, MNRAS, 468, 4956
Zubovas K., King A., 2012, ApJ, 745, L34

SUPPORTING INFORMATION

Supplementary data are available at *MNRAS* online.

Appendix A. Verifying SED fitting procedure.
Appendix B. A detailed assessment of the narrow Hα emission.
Appendix C. Regional [O III] and Hα spectra.
Appendix D. Photometry used in the SED fitting.

Please note: Oxford University Press is not responsible for the content or functionality of any supporting materials supplied by the authors. Any queries (other than missing material) should be directed to the corresponding author for the article.

This paper has been typeset from a TeX/LaTeX file prepared by the author.